Phase separation in lipid-based nanoparticles: exploring the nano-bio interface

Papadopoulou, P.

Citation

Papadopoulou, P. (2023, November 7). *Phase separation in lipid-based nanoparticles: exploring the nano-bio interface*. Retrieved from https://hdl.handle.net/1887/3656645

CHAPTER 5

DOaG-containing mRNA-LNPs specifically target and transfect brain endothelial cells in zebrafish embryos

Parts of this chapter have been used in a research article (currently under revision with Advanced Materials)

Panagiota Papadopoulou#, Winant L. van Os#, Roy Pattipeiluhu, Gabriela Arias-Alpizar, Willem Noteborn, Frederick Campbell, Alexander Kros*

# denotes equal contribution

Abstract | Lipid nanoparticle (LNP) technology has unlocked the potential of mRNA therapeutics, and current developments in the field focus on tissue-targeted therapies for disease-specific treatments. However, cell/tissue selectivity for LNPs, accompanied with efficient mRNA delivery and expression, remain a major challenge. Recently, a liposome formulation containing a diacylglycerol lipid analogue (DOaG), led to specific targeting of brain endothelial cells (bECs) in zebrafish embryos. Here, we investigate whether incorporation of DOaG in LNPs, results in cell-specific mRNA delivery and transfection *in vivo*. By incorporating DOaG – or cholesterol as a control – and by using two different ionizable lipids, four mRNA-LNPs were formulated and demonstrated similar physicochemical characteristics (size, surface charge), and mRNA encapsulation efficiency. Cryo-transmission electron microscopy (cryo-TEM) revealed a phase-separated morphology in DOaG-containing LNPs, similarly to prior developed DOaG-containing liposomes. Subsequently, LNP biodistribution, mRNA delivery and translation were screened in zebrafish embryos and strikingly, DOaG-containing LNPs transfected bECs selectively, depending on the combination with the ionizable lipid. Moreover, transfection was solely observed when specific targeting was involved, in contrast to a shotgun approach where higher transfecting, but non-targeting, formulations did not reveal bEC transfection. Finally, we show that selective delivery of functional oligonucleotides to brain vasculature *is* possible, providing hope for novel drug delivery strategies for brain- and cerebrospinal fluid (CSF) related diseases.

5.1 Introduction

RNA therapeutics are rapidly changing the current landscape of medicine. Gene silencing or gene expression through RNA interference (RNAi) or messenger RNA (mRNA) delivery respectively, could potentially treat a plethora of genetic diseases, develop vaccines, or be used in cancer immunotherapy.[1] Small interfering RNA (siRNA), microRNA (miRNA) and antisense oligonucleotides (ASOs), are short strands of nucleotides that are resilient to *in vivo* degradation and therefore are also suitable as therapeutic agents. Moreover, several techniques are already addressing their inability to diffuse through cell membranes and reach the cytoplasm *i.e.*, conjugation with the sugar moiety GalNac induces receptor mediated endocytosis.[2,3] In contrast, the much larger mRNA is prone to enzymatic degradation by nucleases before entering the cell.[4–6] Therefore, mRNA delivery is critically dependent on lipid nanoparticles (LNPs) which protect RNA from degradation, but also facilitate delivery and endosomal escape to the cytoplasm.[7,8] LNP technology has been in the spotlight after their success in the recent mRNA vaccines against SARs-Cov-2, which was an important milestone for mRNA therapeutics.[9,10] Production, large-scale manufacturing and research of mRNA-LNPs are established and rapidly accelerated.[11] Despite this, due to their high assembly complexity and fairly new development, research with basic information on LNPs is still required, including research on lipid organization, morphology and transfection optimization. For example, the molecular mechanism on LNP assembly was elucidated only recently,[12,13] and LNP morphology as well as racemic pure lipid components, have been addressed to influence the mRNA transfection efficiency.[14–18]

Additionally, existing challenges in nanomedicine, including translational gaps, rapid clearance of lipid-based nanoparticles from systemic circulation, and targeting tissues beyond the liver, can hamper their clinical applicability.[19–21] Therefore, understanding fundamental aspects of LNPs *i.e.*, how lipid composition and physicochemical properties affect their biodistribution,[22] as well as selective uptake and transfection, could facilitate overcoming current challenges.

LNPs have a sophisticated ultrastructure based on the synergistic effect of different lipid components comprising the assembly.[16,22] Components include lipids that provide structural integrity (helper lipids), hydrophobic lipids which reside in the LNP core (structural lipids) and lipids which complex with the nucleic acid cargo (ionizable lipids). Lipid components can individually dictate circulation lifetimes, biodistribution, cell selectivity, or transfection potency [23,24] and therefore rational design of LNPs are of great importance for the outcome of each individual therapeutic. The "helper" lipid, typically a phospholipid, comprises the outer lipid layer exposed to the surrounding environment and dictates surface charge and rigidity.[16] Additionally, a lipid-polyethylene glycol (PEG) conjugate is incorporated on the LNP outer lipid layer, providing structural and long-term stability. Depending on the exact chemistry, PEG lipids can improve circulation lifetimes and/or dissociate from the LNP membrane facilitating desired biodistribution and transfection.[23] The ionizable lipid resides in the solid core of LNPs along with other hydrophobic lipids – *i.e.*, cholesterol -, and mRNA. Having an optimal apparent pKa between 6-7, the ionizable amino lipids can complex with mRNA in acidic pH, followed by LNP assembly and mRNA encapsulation.[25,26] Subsequently, in physiological buffers, ionizable lipids are neutral giving LNPs non-cationic net surface charge, which renders them compatible for clinical use. After LNP endocytosis, ionizable lipids are protonated again in the acidic endosome. In turn, protonated ionizable lipids are thought to electrostatically interact with negatively charged phospholipids of the endosomal membrane, facilitating endosomal disruption and escape of mRNA into the cytoplasm.[27–31] DODAP (1,2-dioleoyl-3-dimethylammonium propane) has been one of the first ionizable synthetic aminolipids developed for nucleic acid encapsulation [26,32] and ever since evolution of the lipid chemistry has led to more potent, clinically approved ionizable lipids for siRNA or mRNA-LNPs *i.e.*, DLin-MC3-DMA (dilinoleylmethyl - 4-dimethyl aminobutyrate, in short MC3), ALC-0315 ([(4-hydroxybutyl)azanediyl]di(hexane-6,1-diyl)bis(2-hexyldecanoate)) or SM-102 (Heptadecan-9-yl-8-((2-hydroxy ethyl)(6-oxo-6-(undecyloxy)hexyl)amino) octanoate).[33–36]

Along with the ionizable lipid, the "structural" lipid mainly occupies the solid core of LNPs. Cholesterol has been extensively used in LNP formulations as a structural lipid due to its hydrophobicity and because it improves circulation lifetimes and facilitates siRNA encapsulation.[37] Additionally, cholesterol exerts the ability to "condense" lipid membranes, pushing them towards the liquid ordered (L_o) phase, increasing stability. Also, it has the propensity to form liquid crystalline phases that can facilitate fusion and transfection.[14,15,38,39] Despite their difference in molecular structure, cholesterol and diacylglycerols (DAGs) exert similar properties in lipid membranes.[40] Due to their hydrophobicity, DAGs mainly reside in between the phospholipid leaflet of the cell membrane. Additionally, they are main components of lipoproteins, especially high-density lipoproteins (HDLs).[41–43] Additionally, DAGs induce condensing effects on lipid membranes (similarly to cholesterol), participate in signaling pathways (*i.e.*, protein kinase C activation) and facilitate protein recruitment.[43–46] Their conical shape perturbs the lamellar structure of a phospholipid bilayer, inducing non-bilayer phases (*i.e.*, inverted hexagonal phase [H_{II}]) and lipid phase separation.[47,48] These in turn can increase the spontaneous negative curvature of membranes, facilitating fusion.[49]

All these properties render DAGs as interesting molecules for lipid-based nanoparticle formulations, nevertheless, have not been explored in LNP development. Recently, the unique properties of DAGs were investigated in a liposomal formulation composed of the synthetic DAG analogue, DOaG (2-hydroxy-3-oleamidopropyl-oleate) and the fully saturated, naturally occurring DSPC (1,2-distearyl-*sn*-glycero-3-phosphatidylcholine).[50] Surprisingly, these liposomes (named PAP3) localized at the brain endothelial cells (bECs) of zebrafish embryos with a great specificity, due to their unique "parachute" liposome morphology. This morphology was a result of lipid phase separation induced by DOaG, creating a lipid droplet within the DSPC leaflet (**Figure 1a**-**c**). bEC targeting was mediated by triglyceride lipases (TGLs), - capillary lumen-bound enzymes highly present in bECs at this developmental stage - facilitating liposome recognition and uptake. Moreover, it was revealed that TGLs specifically recognize and bind to the lipid droplets of PAP3 liposomes, as mediated by higher lipid packing defects due to phase separation.[51] This highlights the influence that lipid organization in membranes has on the nano-bio interface, resulting in cell-specific biodistribution.

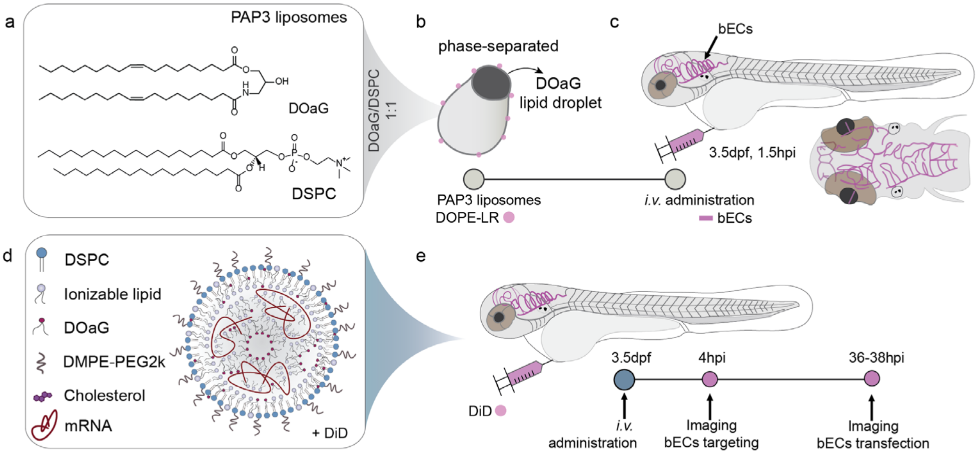

Figure 1. Overview of phase-separated liposomes, mRNA-LNP development strategy, and timeline of experiments. a) Molecular structure of lipids DSPC and DOaG comprising the PAP3 liposomes (in an equimolar mixture). **b)** Schematic of phase-separated morphology of PAP3 liposomes. **c)** Intravenous administration of PAP3 liposomes in 3.5 dpf zebrafish embryos. Brain vasculature depicted in pink, region in which liposomes selectively accumulate at 1.5 hpi. **d)** Schematic representation of an mRNA-LNP and lipids selected for the assembly. Note that cholesterol is not depicted in the LNP schematic. **e)** Timeline of the in vivo assessment of mRNA-LNPs. DOPE-LR = 1,2-dioleoyl-sn-glycero-3-phosphoethanolamine-lissamine rhodamine as a fluorescent tracer, dpf = days post fertilization, hpi = hours post injection.

In this study, we formulated mRNA-LNPs which preferentially target bECs in zebrafish embryos, achieving cell selective mRNA delivery and protein expression. This redirection of nanoparticle biodistribution towards bECs was obtained by replacing cholesterol with DOaG in LNPs, in combination with the ionizable lipid DODAP. Cryo-TEM and cryo-electron tomography (cryo-ET) revealed an unusual mRNA-LNP morphology when DOaG is incorporated in LNP formulations, characterized by two distinct, electron dense, separated phases. This proof-of concept study shows how switching a single lipid component, dramatically affects the morphology and directs biodistribution and transfection of mRNA-LNPs towards specific cell subsets in zebrafish embryos. Finally, this study shows that rational design and selection of lipid composition is important to gain control of nanoparticle *in vivo* behavior.

5.2 Results and Discussion

mRNA-LNPs were successfully formulated with DOaG

Our strategy for the LNP design originates from the DOaG-containing PAP3 liposomes. The two lipid components (DSPC and DOaG) result in phase separation, which leads to bECs specificity in zebrafish embryos (**Figure 1a-c**). Therefore, formulating mRNA-LNPs incorporating DOaG as a structural lipid component could result in formulations that preferentially target bECs of zebrafish embryos, with concomitant mRNA delivery and protein expression. Based on LNP formulations containing standard lipid components (*i.e.*, helper, structural and ionizable lipids), we designed DOaG-based mRNA-LNPs and their biodistribution, bEC targeting, and mRNA expression was qualitatively and quantitively studied in transgenic zebrafish embryos (**Figure 1 d, e**).

Four formulations were designed for the study (**Figure 2a, b)**, investigating the effect of two different ionizable lipids (DODAP and the clinically approved MC3) and replacing the structural lipid cholesterol with DOaG. In all formulations, DSPC was chosen as the helper lipid and the short-chain DMPE-PEG2k was used as the PEG lipid, which is known to desorb from the LNP surface *in vivo*, enabling nanoparticle - protein interactions.[23] LNPs were formulated encapsulating functional mRNA expressing fluorescent reporter protein mCherry, using a Nitrogen to Phosphate ratio of 6 (N/P = 6) (**Figure 2c**). Reporter protein mCherry was preferred over GFP due to its decreased autofluorescence levels (**Figure S1)**, allowing for broader range of fluorescence intensity measurements. For the real time biodistribution studies, all LNPs contained the far-red lipophilic dye DiD (1,1′-dioctadecyl- 3, 3, 3′, 3′ - tetramethylindodicarbo cyanine, 4- chlorobenzene sulfonate). The *kdrl*:GFP zebrafish line (GFP-positive vasculature) was used for vasculature visualization and colocalization studies. All LNPs were fully characterized and found to have properties with comparable values in size, charge, PDI and encapsulation efficiency. LNPs were characterized by dynamic light scattering (DLS) and were found in the range of 100.5-148.4 nm in average hydrodynamic diameter, low polydispersity indices and near neutral to slightly anionic surface charge (**Figure 2d, e**). Additionally, encapsulation efficiency (%EE) of mRNA was high for all formulations (**Figure 2f**). In summary, replacing cholesterol with DOaG does not significantly alter the LNP assembly, physicochemical properties and mRNA %EE. Hereafter, we use the following nomenclature for the four LNP formulations: LNP-A (*i.e.,* CHO-DODAP), LNP-B (*i.e.,* DOaG-DODAP), LNP-C (*i.e.,* CHO-MC3) and LNP-D (*i.e.,* DOaG-MC3) (**Figure 2b**).

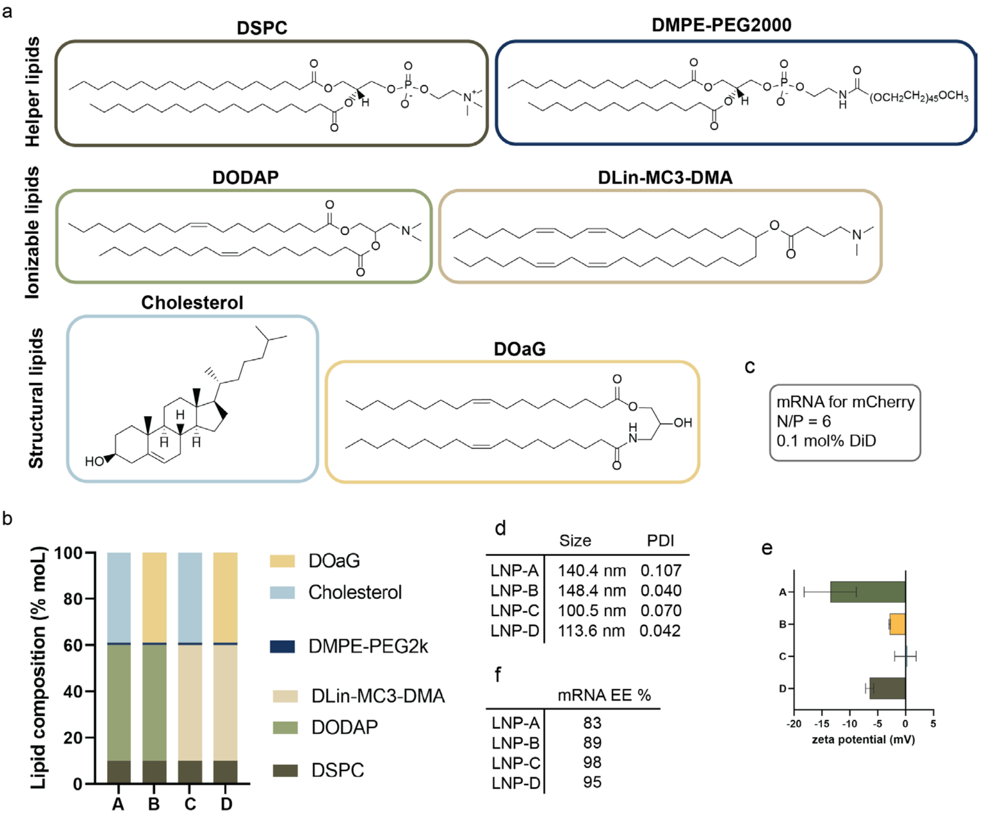

	Size	PDI
LNP-A	140.4 nm	0.107
LNP-B	148.4 nm	0.040
LNP-C	100.5 nm	0.070
LNP-D	113.6 nm	0.042

	mRNA EE %
LNP-A	83
LNP-B	89
LNP-C	98
LNP-D	95

Figure 2. Lipid composition of mRNA-LNP formulations and physicochemical properties. a) Molecular structures of lipid components used for mRNA-LNPs. **b)** Molar ratios of lipid components and composition of the four mRNA-LNP formulations. **c)** Information on functional mRNA, N/P ratio and fluorescent tracer, constant for all LNP formulations. **d)** Size (average hydrodynamic diameter) and PDI of mRNA-LNP formulations as determined by DLS. **e)** Surface charge of LNP formulations, as determined by zeta-potential measurements. **f)** Encapsulation efficiency of mRNA of all mRNA-LNP formulations. e demonstrates three technical replicates.

Cryo-TEM reveals phase-separated morphology on DOaG-based mRNA-LNPs

Previously, PAP3 liposomes were found to accumulate in bECs as a result of their phase-separated morphology.[50] Being a two-component lipid system, it was easy to manipulate molar ratios, revealing that lipid droplets in liposomes were only observed after DOaG reached the phase separation threshold in the membrane. Interestingly, the selective *in vivo* targeting of liposomes to the bECs corelated with phase separation. Thus, morphology played a pivotal role on bEC specificity and therefore we sought to investigate whether DOaG also induced a unique morphology in LNP formulations. Cryo-TEM and cryo-ET was used to assess LNP ultrastructure and identify differences in morphology between all LNP formulations. For LNP-A, most of particles were either solid, or nanoparticles with distinct lamellar lipid compartments, possibly composed of a phospholipid bilayer (**Figure 3a black arrow** and **Figure S2**). Such structures have been previously described as lipid "blebs" for LNP compositions similar to LNP-A, and RNA has been found to localize in the "bleb's" hydrophilic core.[13,52] For LNP-A, a distinct punctuated electron-dense pattern is observed in the hydrophilic core of the bleb, indicating similarly mRNA localization (**Figure 3a, red arrow**). The morphology of LNP-C is characterized by solid lipid particles with a multilamellar lipid partitioning observed for some of the particles (**Figure 3c** and **Figure S2**). This type of morphology for similar lipid compositions has been described before.[53] Interestingly, the DOaG containing LNPs (LNP-B and LNP-D) were found to be solid, however a phase-separated droplet with different electron density was present within the solid particles (**Figure 3b, d** and **Figure S2**). Cryo-ET of LNP-B revealed the morphology in higher resolution, and a bilayer around the phase-separated droplet could be observed **(Figure 3e-g**). It is not known whether this bilayer consists of one or more lipid components. A similar morphology has been recently characterized, where cholesterol was replaced by its analogue fucosterol.[15] It was suggested that phase separation may influence the mRNA localization towards the protruded area, however, no conclusive data was presented to support this claim. The electron density observed in the separate droplet in LNP-B and D is similar to the electron density induced when mRNA is present, which suggests that mRNA is present in the phase-separated droplet.

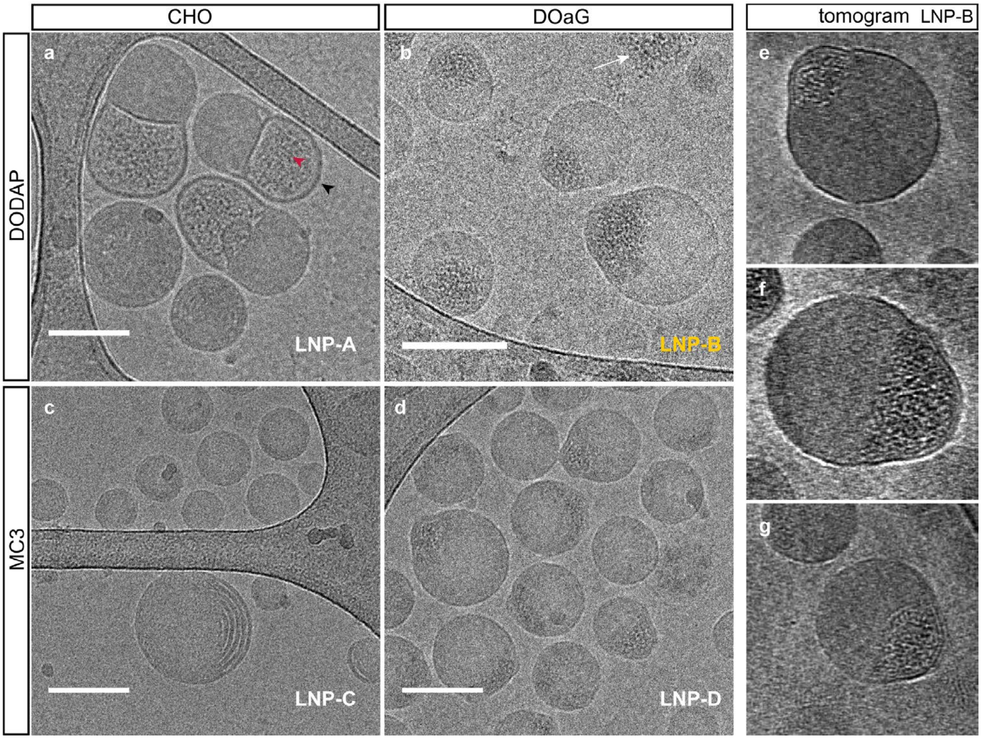

Figure 3. Cryo-electron microscopy images of mRNA-LNP formulations. Cryo-TEM images of **a)** LNP-A, **b)** LNP-B, **c)** LNP-C, **d)** LNP-D. **e-g)** Cryo-ET images of LNP-B. **f** is a cross section. Black arrow depicts the phospholipid bleb. Red and white arrows possibly depict encapsulated and free mRNA, respectively, as described before.[13] Scale bars: 100 nm.

DOaG-DODAP containing LNPs target the bECs of zebrafish embryos

All four LNP formulations shared similar physicochemical properties (size range, PDI, surface charge) allowing us to assess the LNPs' potential to target bECs based on difference in lipid composition and/or morphology. Formulations were intravenously (IV) administered in zebrafish embryos at 3.5 days post fertilization (dpf) and imaged in real time with confocal microscopy (**Figure 4a**). All formulations, revealed to be predominantly in circulation 4 hours post injection (hpi) (**Figure 4b** and **Figure S3a, c, e, g**). To investigate bEC targeting in more detail, cellular localization of LNPs was studied by high resolution confocal z-stack imaging at the hindbrain, from a dorsal perspective (insert **Figure 4a, Figure 4c**). LNP-A and C revealed to be circulating represented by a haze of

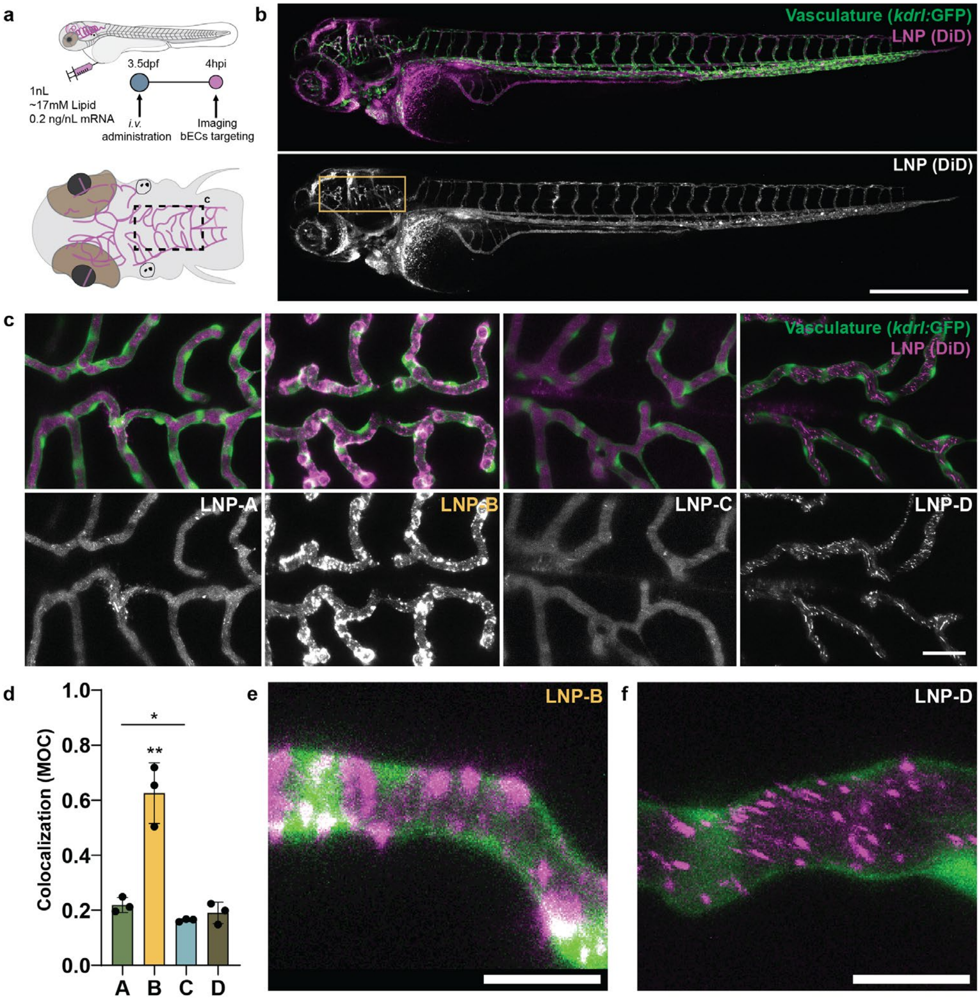

Figure 4. Biodistribution of mRNA-LNPs within zebrafish embryos (3.5 dpf). a) Timeline of experimental setup. **b)** Lateral view on 3.5 dpf zebrafish embryo revealing DiD-represented biodistribution (4 hpi) as an overlay of LNP-B (magenta, single channel white) and GFP positive vasculature (green). Yellow box indicates region of brain vasculature. **c)** Dorsal view on brain vasculature at 4 hpi revealing biodistribution of LNP-A, LNP-B, LNP-C and LNP-D. **d)** Quantification of Mander's Overlap Coefficient (MOC) for DiD signal in relation to GFP-positive vasculature. **e)** LNP-B (magenta) reveals colocalizing clusters with GFP-positive vasculature (green) in contrast to **f)** LNP-D which display clusters in the vasculature lumen. Scale bars: 500 µm (b), 25 µm (c), and 10 µm (e, f). Statistical significance was evaluated as ns: not significant ($p > 0.05$), significantly different *$p < 0.05$, **$p < 0.01$; ***$p < 0.001$. Note that B is significantly different to A, C and D. Exact p-values: A-B = 0.0034, A-C = 0.0263, A-D = 0.3533, B-C = 0.0019, B-D = 0.0030, C-D = 0.3081.

fluorescence within the vasculature lumen (**Figure 4c**). Formulation LNP-D, also revealed to be circulating freely (**Figure S3g**), however in a likely aggregated state represented by clusters localized in the vasculature lumen (**Figure 4c, f**). Strikingly, LNP-B revealed also strong fluorescent clusters, however these were localizing at the bECs, in contrast to LNP-D (**Figure 4c, e**). These dense localizations of DiD could be interpreted as either the result of LNP aggregation at the bECs *or* endosomal uptake. As bECs have a thickness close to the diffraction limit, excluding whether clusters remain intra- or extracellular was limited. Nonetheless, the combination of GFP-positive vasculature and far-red labeled LNPs allowed for quantification of their colocalization by using the Manders' Overlap coefficient (MOC) (**Figure 4d** and **Figure S3b, d, f, h**).[54] Quantification (n = 3) revealed that DiD labeled LNP-B localized preferentially at the bECs, compared to the other LNP formulations ($p<0.01$). This suggests an important, though not decisive, role for both ionizable lipid, as well as DOaG, in LNP-mediated cell selective targeting (no targeting for LNP-D). Moreover, as cryo-TEM revealed similar morphologies for LNP-B and LNP-D, it is suggested that phase separation does not warrant bEC targeting, however appears to be an important component for it, since non-phase separated formulations (LNP-A and C) do not reveal any targeting.

LNP targeting is required for transfection

To assess whether bEC-targeting of LNP-B results in local translation of its mRNA-cargo, we investigated the expression of mCherry protein at 36-38 hpi (**Figure 5a**). Whole fish and head were visualized for transfection **(Figure S4a, b, d, e, g, h, j, k**). Though visualized at n=1, it is worth noticing three findings from these acquisitions. First, DODAP containing formulations revealed overall relatively lower transfection levels in comparison to MC3 containing formulations (**Figure 5c** and **Figure S4a, b, d, e** compared to **4g, h, j, k**). This is in line with literature, where MC3 – compared to DODAP – has been demonstrated as a more potent ionizable lipid resulting in high transfection levels.[33] Secondly, LNP-C revealed high levels of transfection at the head and around the liver-swim bladder (**Figure 5c** and **Figure S4g, h**).

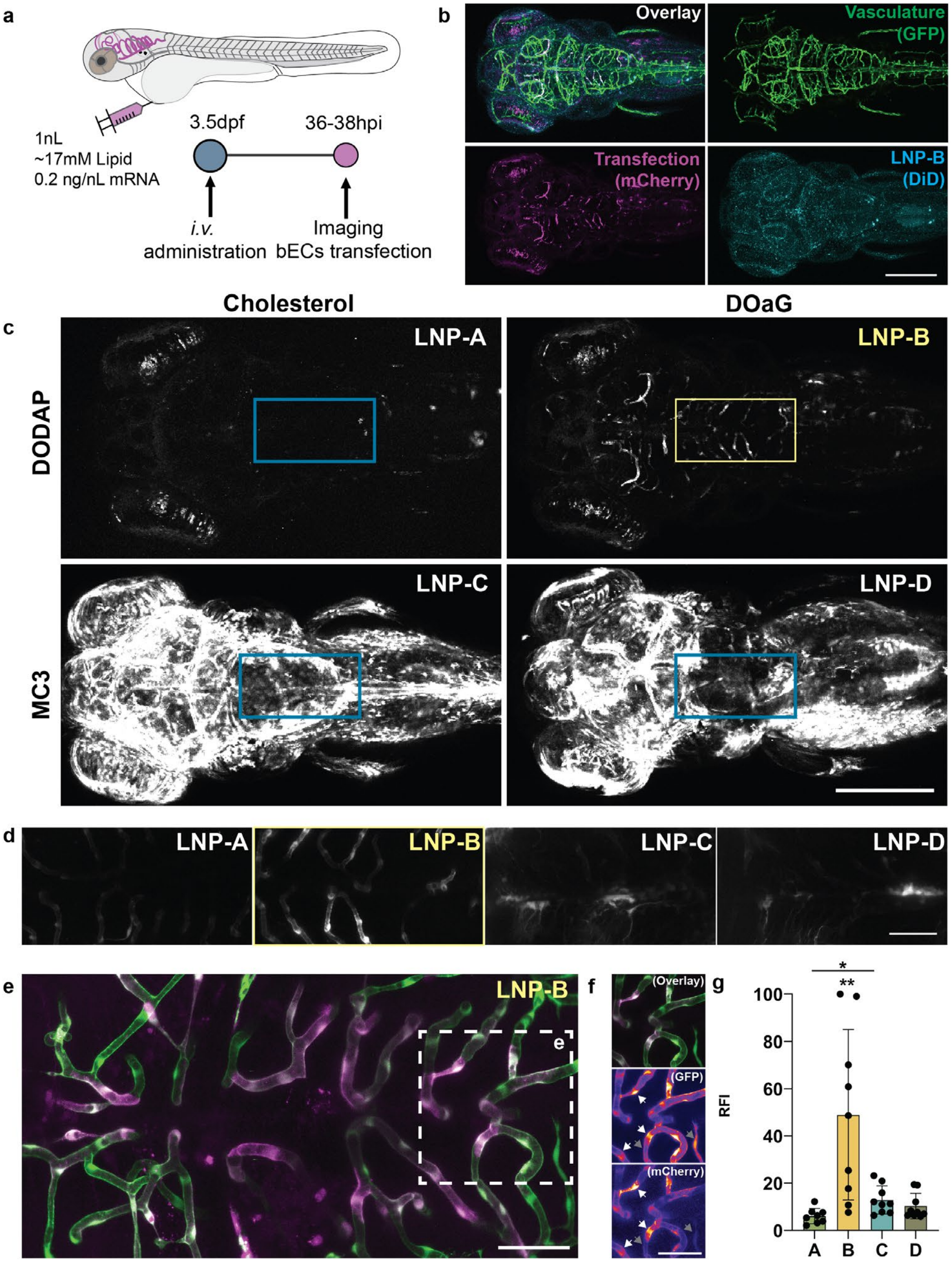

Figure 5. Transfection of zebrafish bECs by mRNA delivery mediated by the different LNP formulations. a) Schematic timeline of experimental setup. **b)** Dorsal view on the embryo's head 36-38 hpi of LNP-B, revealing GFP-positive vasculature (green), mCherry expression as result of transfection (magenta), DiD biodistribution (cyan) and overlay. **c)** mCherry expression as a result of transfection for each formulation in the head region of

the fish. **d)** Insets of (c) depicting confocal z-stacks of brain vasculature regions used for quantification studies. **e)** Overlay of mCherry expression (as mediated by LNP-B) and transgenic GFP positive vasculature. **f)** Inset of (e) depicting co-localization of GFP and mCherry (white arrows) and independent GFP fluorescence (gray arrows) indicating fluorescence as a result of transfection, not channel bleed-through **g)** Quantification of mCherry relative fluorescence intensity as a result of bECs transfection, per formulation. Scale bars: 250 µm (b, c) and 50 µm (d, e, f). Statistical significance was evaluated as ns: not significant ($p > 0.05$), significantly different *$p < 0.05$, **$p < 0.01$; ***$p < 0.001$. Note that B is significantly different to A, C and D. Exact p-values: A-B = 0.0045, A-C = 0.0113, A-D = 0.0742, B-C = 0.0093, B-D = 0.0059, C-D = 0.3460.

For LNP-C, 3D imaging of the head visualized mCherry expression rather at the exterior site of the brain, likely localized at the skin. Third, although with a lower Relative Fluorescence Intensity (RFI) than LNP-C and D, LNP-B revealed mCherry emission in the brain region from both lateral and dorsal perspective (**Figure S4d, e**). A more detailed view at the brain vasculature (n=9) confirmed that mCherry expression in the head, as mediated by LNP-B, is indeed localized at the bECs with relatively high expression levels of transfection (**Figure 5c, d**). Differing fluorescent intensity- and/or localization profiles (e.g., GFP, mCherry, and DiD) excluded the potential of major channel bleed-through (**Figure 5b**). In contrast, LNP-A, C and D did not seem to result in transfection in bECs, as mCherry fluorescence was very low and likely present as a result of GFP bleed-through (**Figure 5d**). For LNP-B, high-resolution imaging revealed colocalization between GFP positive vasculature and mCherry transfection (**Figure 5e**), displaying specific (non-bleed-through) individual bEC transfection (**Figure 5f**, white arrow for GFP and mCherry positive, grey arrow for only GFP positive). Quantification (n = 9) revealed that mCherry expression in bECs is significantly higher for LNP-B than LNP-A, C and D ($p<0.01$, **Figure 5g** and **Figure S4c, f, i, l**). In summary, LNP-B results in specific bEC targeting compared to non-targeting LNP-A and non-targeting - but highly transfecting - LNP-C and D. Together, this study indicates that specific targeting of bECs in zebrafish embryos is required for mRNA delivery resulting in concomitant protein expression.

5.3 Discussion and Conclusion

This work describes an LNP screening study in zebrafish embryos, in which novel DOaG-containing mRNA-LNPs (LNP-B) are found to selectively target the embryos' bECs, a subset of endothelial cells. After the selective targeting and accumulation of LNPs, selective mRNA delivery, bEC transfection, and concomitant protein expression is observed. Although two of the formulations achieve higher transfection levels throughout the whole fish (LNP-C and D), they lacked selective bEC transfection. This highlights that cell specific LNP targeting is required for cell specific mRNA delivery and translation, in contrast to a shotgun approach where tissue of interest is usually exposed to non-specific, highly potent nanomedicines.

Furthermore, replacement of cholesterol with DOaG resulted in LNPs that target bECs, indicating a potential role of DOaG for this selectivity. However, to achieve selective accumulation, clustering in circulation should be avoided. This is because the two DOaG-containing LNPs (LNP-B and LNP-D) revealed opposing biodistribution patterns, where the non-targeting LNP-D seemed to cluster in circulation, suggesting colloidal instability *in vivo*. Here, the transparent zebrafish model, which enables real time imaging, allowed us to conclude that to achieve cell specific targeting, colloidal stability of LNPs *in vivo* is an important requirement.

Moreover, this proof-of-concept study highlights that switching one only lipid component dramatically affects the LNP biodistribution (*i.e.*, DOaG vs. cholesterol). Similarly, replacing DODAP with MC3 results in a formulation (LNP-D) that cannot achieve cell specific targeting, probably due to clustering in circulation. This suggests that DOaG-related specificity is achieved in combination with the ionizable lipid DODAP. This opens new avenues for exploring different lipid ratios between the LNP-B lipid components, or combinations of DOaG and/or DODAP with different - ideally more potent - ionizable lipids, to enhance the transfection potency. Overall, understanding the effects of lipid composition on LNP properties is vital for rational nanoparticle design. Especially for multicomponent systems such as LNPs, ultrastructure, stability and overall physicochemical properties are a result of specific lipid packing, and therefore a one-fits-all approach for design should not be utilized.

Interestingly, DOaG-containing LNP-B promotes cell selective biodistribution in zebrafish embryos with a yet unknown mechanism. Given that TGL plays a role on selective bEC targeting by DOaG-containing liposomes (PAP3) as previously described,[50] it is likely that a similar mechanism is involved in the LNP-B uptake. However, experiments will have to be conducted to prove this hypothesis.

Although the novel morphology of LNP-B may contribute to the bEC targeting, it is very important to note that LNP-B and D have a very similar macromolecular structure. LNP-B targets the bECs with relatively high specificity, whereas LNP-D is presented as clusters in circulation. We hypothesize that there is a molecular difference between those two formulations that is beyond the resolution of cryo-TEM. This difference at the molecular level could contribute to the clustering of LNP-D which prevents accumulation in bECs. Further studies are required to elucidate the mechanism of targeting and whether the phase-separated LNP morphology is essential.

DAGs are lipids with several interesting properties including fusion promotion, polymorphism, and according to this and our previous studies,[50,51] protein recruitment and cell selectivity. One potential advantage of using DAGs as lipid components in LNPs, is their propensity to form inverse hexagonal phases which can potentially facilitate endosomal escape, leading to higher transfection efficiencies. Also, their general ability to induce phase separation in LNPs could propel higher transfection potencies, similarly to recently described phase-separated blebs in LNP systems.[55]

The initial discovery of phase separation as a novel targeting concept [50] resulted in the development of a second-generation formulation (mRNA-LNP). Combined with previous studies[24,56–58] we demonstrate that zebrafish embryos is a robust *in vivo* screening model for the discovery or bottom-up development of nanoparticle formulations with an enhanced *in vivo* function. This is because zebrafish offer the ability to observe nanoparticle biodistribution and behavior in real time and at a cellular level. Based on a workflow involving thorough nanoparticle characterization (size, polydispersity, charge, morphology, cargo-loading) in combination with this screening model/tool, we have developed mRNA-LNPs that specifically transfect bECs in zebrafish embryos. Additional research is needed to investigate whether the selective gene delivery in zebrafish bECs is translatable in mammalian animals. Previously on a mouse study, rapid clearance of PAP3 liposomes in organs such as the liver and spleen was observed. [50] Similar clearance may be expected for LNP-B, however, given that LNP-B is more stable than PAP3 liposomes (stable for at least up to 1 month compared to ~7 days) (**Figure S5**) it may circumvent rapid clearance and exhibit different biodistribution patterns. However, if a TGL mediated pathway is involved as with PAP3 liposomes, it is likely that organs such as the liver, but also heart and reproductive organs, may be targeted.

Achieving selective delivery of *functional* oligonucleotide cargo to brain vasculature in zebrafish embryos, demonstrates the potential for disease specific therapies based on design of cell selective LNPs. Although these studies have been performed in only one type of species and differences in expression may be expected across species,[59] the zebrafish embryo can be the starting point for translational studies. Nonetheless, the fact that transfection of brain vasculature *is* possible, provides hope and potential for novel drug delivery strategies for brain- and CSF related diseases. Oligonucleotide delivery to brain vasculature could serve as a *trojan horse* by having brain endothelium selectively produce and secret therapeutic proteins (*e.g.*, monoclonal antibodies[60] or growth factors[61]) at the basolateral side into CSF, thereby reaching brain (diseased) tissue. Recent endeavors support this strategy,[62] where endothelial-specific mouse adeno-associated virus capsids were used to genetically engineer the blood-brain barrier into a functional ‘biofactory’ to rescue synaptic deficits. Another approach would encompass mRNA- and/or siRNA delivery to brain endothelial cells and could (back) gain control over brain homeostasis in diseased states,[63] thereby providing opportunities for novel, future RNA-based therapies.

In summary, we have successfully demonstrated selective transfection of brain endothelial cells *in vivo*, based on LNP cell-selective targeting. This proof-of-concept LNP formulation provides an intersection from which parallel routes can be taken, including investigation of bEC gene expression/suppression at embryonic stages, translational and mechanistic studies, formulation optimization, structure-activity relationship studies in combination with Cryo-TEM, and exploration of potential role of diacylglycerol lipids in the field of nanomedicine.

5.4 Materials and Methods

General reagents: 1,2-distearoyl-*sn*-glycero-3phosphocholine (DSPC), 1,2-dioleoyl-3-dimethylammonium-propane (DODAP), CHO and DMPE-PEG2k were purchased from Avanti Polar Lipids. Additional DSPC was purchased from Lipoid GmbH. MC3 was purchased from Biorbyt. 1,1'-Dioctadecyl-3,3,3',3'-Tetramethylindodicarbocyanine, 4-Chlorobenzenesulfonate Salt (DiD) was purchased from Thermo Fisher Scientific. mCherry mRNA (CleanCap®, 5moU, 1 mg/mL in 1 mM Sodium Citrate pH=6.4) was purchased from Trilink Biotechnologies, aliquoted in nuclease-free Eppendorf tubes and stored at -80 °C. All other chemical reagents were purchased at the highest grade available from Sigma Aldrich and used without further purification. All solvents were purchased from Biosolve Ltd. Ultrapure MilliQ® water, purified by a H_2O Advantage A10 water purification system from MilliPore, was used throughout. Nuclease-free Ultrapure MilliQ® water was made in house.

Synthesis of DOaG lipid: DOaG lipid was synthesized as reported in Chapter 2.

LNP formulation: Encapsulation of mRNA and simultaneous formation of lipid nanoparticles in a Nitrogen to Phosphate ratio (N/P ratio) of 6, was performed as previously described.[24] In brief, individual lipid components (DSPC, DMPE-PEG2k, DOaG or CHO, DODAP or MC3) as stock solutions in chloroform (1-10 mM), were combined to the desired molar ratios and dried to ensure complete removal of chloroform, first under a stream of N_2, then >1 h under vacuum. The non-exchangeable tracer DiD was also added to the lipid mixtures at a total lipid concentration of 0.1% mol. Lipid films were re-dissolved (with vortrexing) in 200 μL of absolute ethanol at a total lipid concentration of 5.31 mM. In another vial, 30 μL of mRNA encoding mCherry (1 mg/mL) were diluted up to 600 μL with nuclease-free sodium citrate buffer (pH 4, 16.7 mM trisodium citrate dihydrate and 30.5 mM citric acid monohydrate). Controlled rapid mixing of the two solutions was achieved by using a custom-made T-junction mixer, equipped with syringe pumps (fusion 100-X, Chemyx Inc., Stafford, USA) and syringes with an inner diameter of 4.78 mm. The total flow rate was 2 mL/min, with a flow rate ratio of 3:1 v/v citrate buffer: ethanol). The resulting LNP formulations were dialyzed overnight against nuclease-free PBS (pH=7.4). After that, they were concentrated at 4 °C to the lowest volume possible by centrifugation at 2000-3000 g using 100K MWCO centrifugal filters (Amicon® Ultra, Merck) resulting in mRNA-LNPs with [total lipid] ~16-18 mM. Microfluidic mixing and mRNA were handled with nuclease-free lab consumables and gloves throughout.

Encapsulation efficiency and mRNA concentration determination after LNP formation: Encapsulation efficiency and mRNA concentration were determined using the high range assay of Quant-iT™ RiboGreen® RNA assay kit (Invitrogen®, ThermoFisher Scientific) with nuclease-free TE buffer throughout. Briefly, to determine the unencapsulated mRNA [$\mathrm{mRNA}_{\mathrm{free}}$] in the sample, 10 μL of each LNP formulation (100x diluted with nuclease-free, filtered PBS) was added in a 96 well plate (Greiner, black). To determine the total mRNA in each sample [$\mathrm{mRNA}_{\mathrm{total}}$], 10 μL of each formulation was added to wells mixing in 10 μL of 1% triton X-100 (prepared with nuclease-free H_2O). The samples were diluted to 100 μL with TE buffer and subsequently 100 μL of RiboGreen reagent was added. Fluorescence intensity (λ_{ex} = 485 nm, λ_{em} = 530 nm) was determined using a fluorescence microplate reader (Infinite®, M1000 pro, TECAN) 5 min after adding the RiboGreen reagent. The mRNA concentration (mg/ml) was determined for every individual experiment using a calibration curve. Encapsulated mRNA was determined with the following equation: [$\mathrm{mRNA}_{\mathrm{encapsulated}}$] = [$\mathrm{mRNA}_{\mathrm{total}}$] – [$\mathrm{mRNA}_{\mathrm{free}}$] and encapsulation efficiency by: EE% = $\left(\frac{[mRNAencapsulated]}{[mRNAtotal]}\right)$ x 100%. All measurements were conducted in triplicate. All preparations were handled with nuclease-free lab consumables and gloves throughout. For administration in embryonic zebrafish ($V_{\mathrm{injection}}$ = 1 nL) the LNP formulations were diluted to contain [mRNA] = 0.2 mg/mL.

Size and zeta potential measurements: Particle size and PDI values were obtained by using a Malvern Zetasizer Nano ZS. DLS measurements (operating wavelength = 633 nm), were carried out at room temperature in PBS (pH=7.4) at a [total lipid] = 100 μM. Zeta potential of each LNP formulation was measured at [total lipid] = 500 μM, using a dip-cell electrode (ZEN1002, Malvern), at room temperature and at [NaCl] <20 mM. All reported DLS and zeta potential measurements are the average of three measurements.

Cryogenic transmission electron microscopy: mRNA-LNP formulations (3.5 µL) were applied to a freshly glow-discharged carbon 200 mesh Cu grid (Lacey carbon film, Electron Microscopy Sciences, Aurion, The Netherlands). Grids were blotted for 3 s at 99% humidity in a Vitrobot plunge-freezer (FEI VitrobotTM Mark III, Thermo Fisher Scientific), with a waiting time of 30 sec before blotting. Cryo-TEM images were collected on a Talos L120C (NeCEN, Leiden University) operating at 120 kV, equipped with a Ceta camera and LaB6 filament. Images were recorded manually at a nominal magnification of 11000 or 13500x for low magnification images yielding a pixel size at the specimen of 9.47 or 7.44 ångström (Å), respectively. For high magnification images a nominal magnification of 28000 or 36000x was used, yielding a pixel size at the specimen of 3.46 or 2.84 ångström (Å), respectively.

Cryo-electron tomography: Cryo-ET was performed on a Titan Krios microscope operating at 300 kV equipped with a K3 direct electron detector and BioQuantum energy filter (NeCEN, Leiden University). Tilt series were collected without the use of fiducials with SerialEM[64] at a nominal magnification of 19500x (4.4 Å/pixel) and 42000x (2.17 Å /pixel), respectively, using a dose-symmetric tilt scheme from -50° to 50° with 2° increments and a total dose of 100 e-/ Å^2. Tomograms were reconstructed using the IMOD software package.[65]

Zebrafish husbandry and injections: Zebrafish (*Danio rerio*, Tg (*kdrl*:GFP)^{s843})[66] were, in compliance with the directives of the local animal welfare committee of Leiden University, handled and maintained according to Zebrafish Model Organism Database guidelines (http://zfin.org, 2023). Natural spawning at beginning of light period was used for fertilized egg collection, which were subsequently grown at 28.5 °C in egg water (60 g/ml Instant Ocean Sea salts). Zebrafish embryos were anesthetized and embedded in 0.4% (w/v) agarose containing 0.01% tricaine. Screening studies from injection to image analysis were kept blind. Formulations were injected in the Duct of Cuvier at 3.5 dpf stage as previously described [67] ($V_{injection}$ = 1 nL volume, [mRNA] = 0.2 mg/mL per embryo). Zebrafish were qualified as correctly injected when formulation fluorescence correlated with vasculature and no backward translocation of erythrocytes and/or yolk damage was detected. Fish were randomly selected from a group of correctly injected embryos. Confocal microscopy was performed at 4 hpi and 36-38 hpi and embryos were imaged by overlapping z-plane. Images for quantification were performed using a Leica TCS SP8 confocal microscope, with a 40X water-immersion objective (HCX APO L) and photon count as detection method. Laser intensity, gain, and offset settings were kept identical for unbiased quantification.

Confocal imaging and processing: Images were processed using software (Fiji) ImageJ 2.9.0/1.53t; Java 1.8.0_172 (64- bit). To enhance visualization of the biodistribution in lateral 10× images, mCherry/DiD channel 'Diplay Range Max' was manually optimized; for 40X quantification all settings were kept equal. For targeting studies (4 hpi, DiD channel) number of embryos per group was kept at n=3 due to logistic trade-off in imaging time and hpi, whereas for transfection studies (36-38 hpi, mCherry channel) number of embryos per group was set at n=9. Number of embryos for group A was n=8, as one of the injected embryos was excluded due to damaging of the embryo during transfer.

Quantification of bEC targeting and transfection: Quantification was performed as described in macros using Fiji (see Supplementary Information). Briefly, two methods of quantification were performed: i) GFP positive bEC colocalization with DiD at 4hpi, and ii) quantification of mCherry Fluorescence Intensity that colocalized with GFP positive bEC. For first colocalization studies images were processed in Fiji using Plugin "JACOP" [68] and expressed in a bar plot as a result of MOC. For transfection studies, a mask was created as described in macro, to exclude bEC-negative mCherry from quantification, whereafter leftover fluorescence intensity was quantified and displayed as RFI in a bar plot.

5.5 Supplementary Information

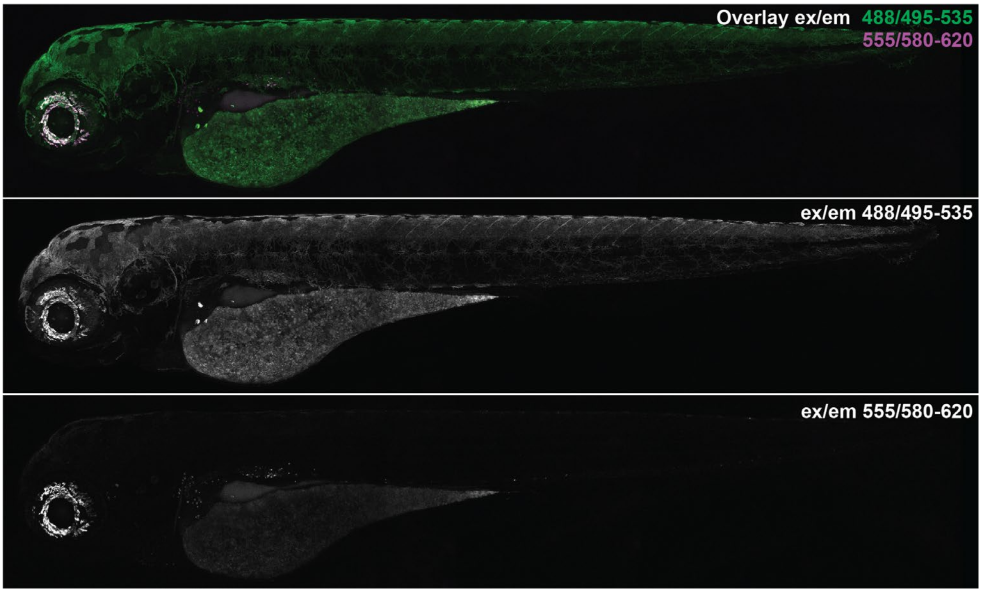

Figure S1. Autofluorescence levels of a 3.5 dpf ABTL zebrafish embryo (wild type) in green (ex/em: 488/495-535 nm) and red channels (ex/em: 555/580-620 nm) and overlay thereof.

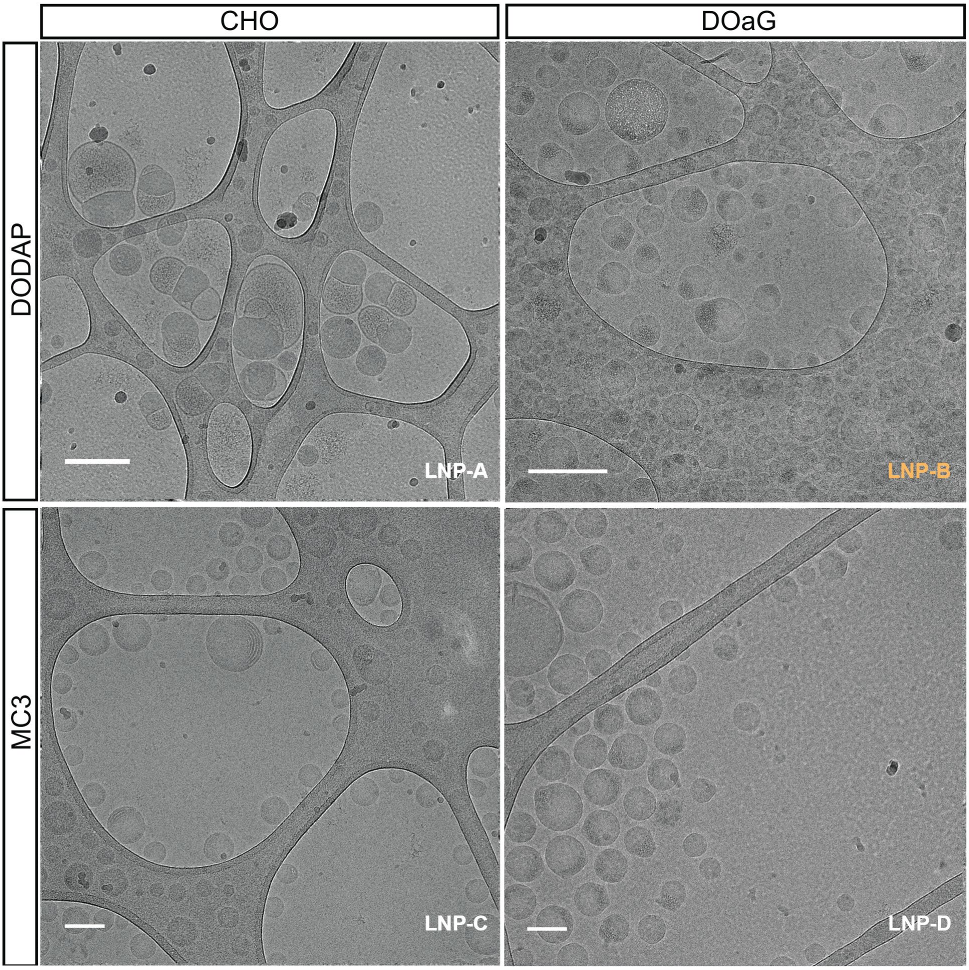

Figure S2. Low magnification Cryo-TEM images of LNP formulations, LNP-A, B, C and D. Scale bars: 200 nm.

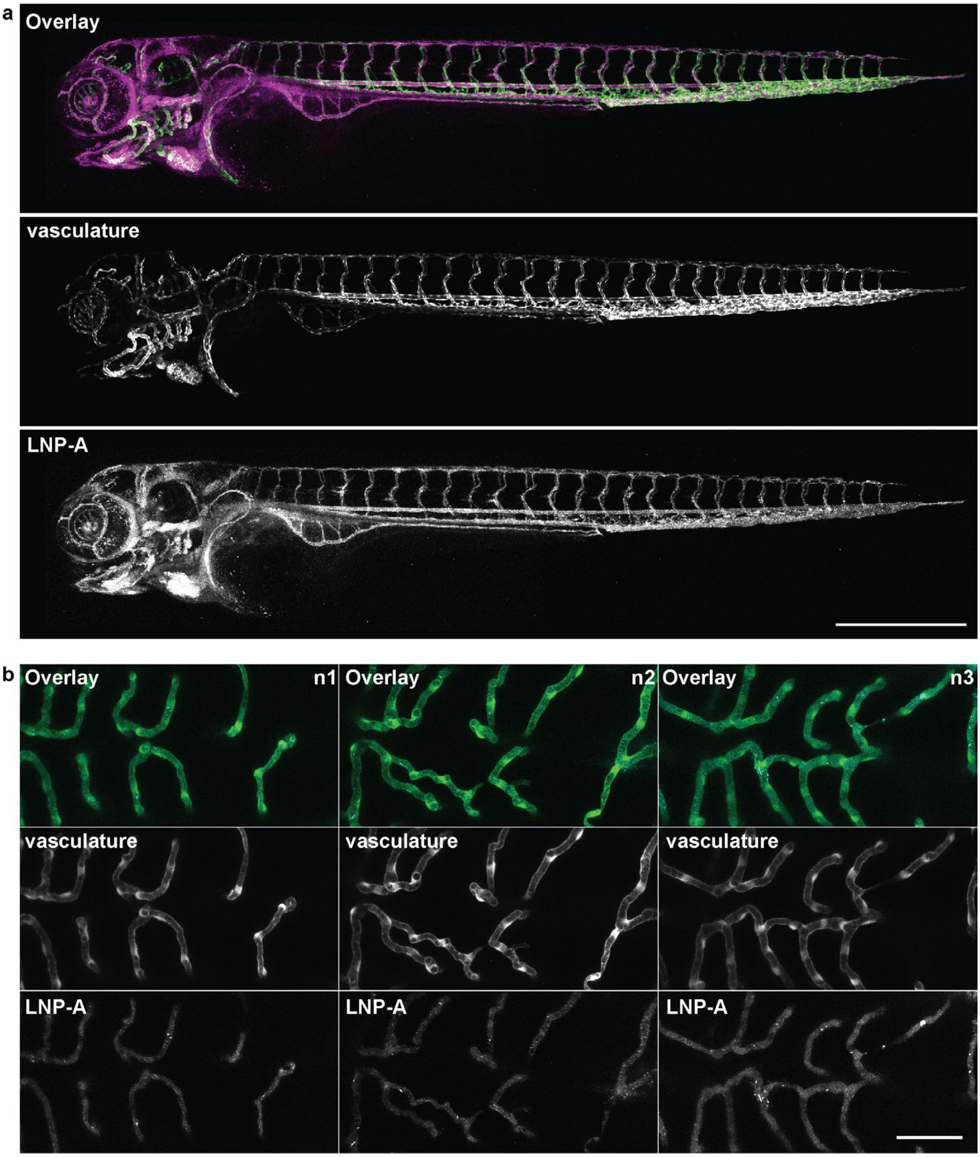
a
Overlay
vasculature
LNP-A
b
Overlay
n1
Overlay
n2
Overlay
n3
vasculature
vasculature
vasculature
LNP-A
LNP-A
LNP-A

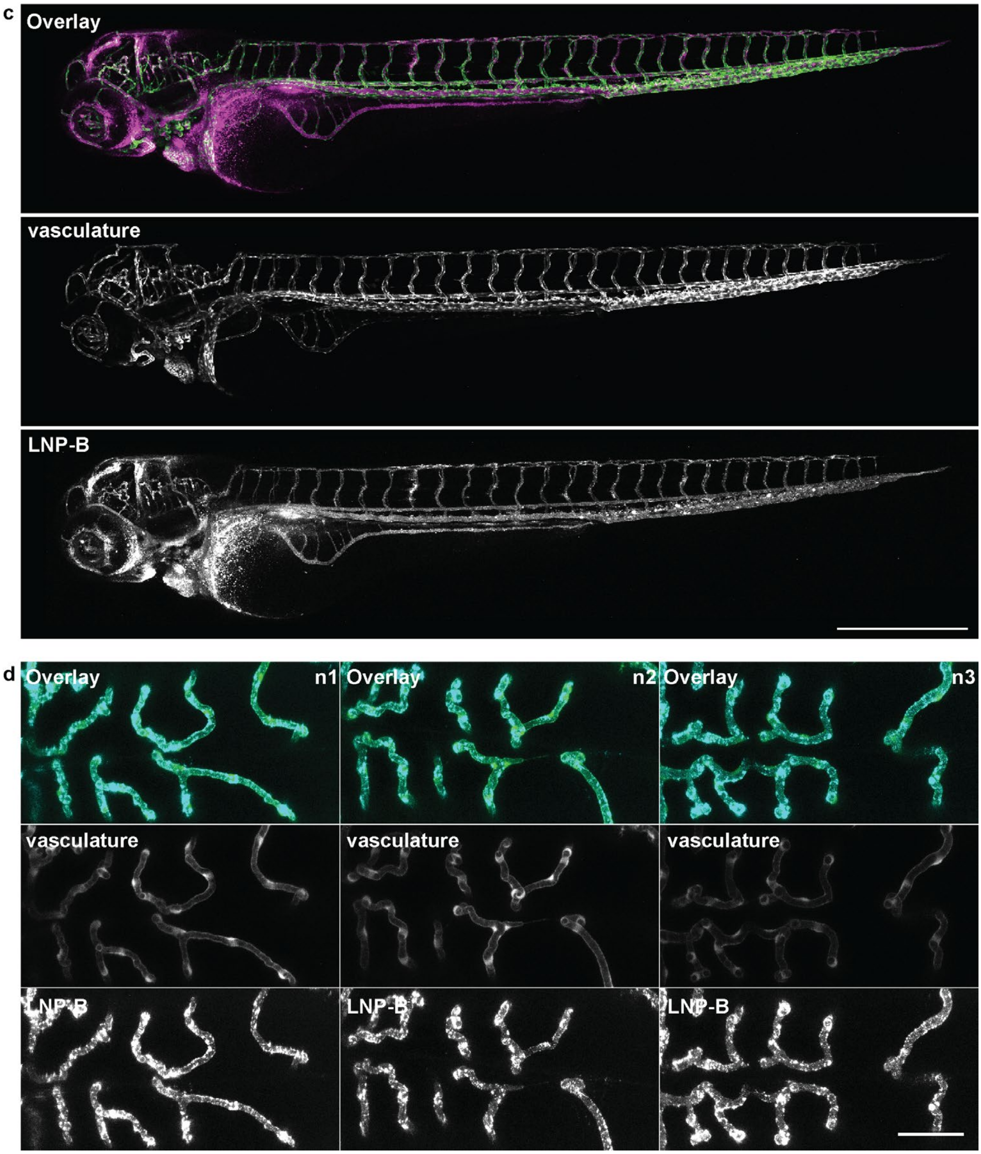
c
Overlay
vasculature
LNP-B
d
Overlay
n1
Overlay
n2
Overlay
n3
vasculature
vasculature
vasculature
LNP-B
LNP-B
LNP-B

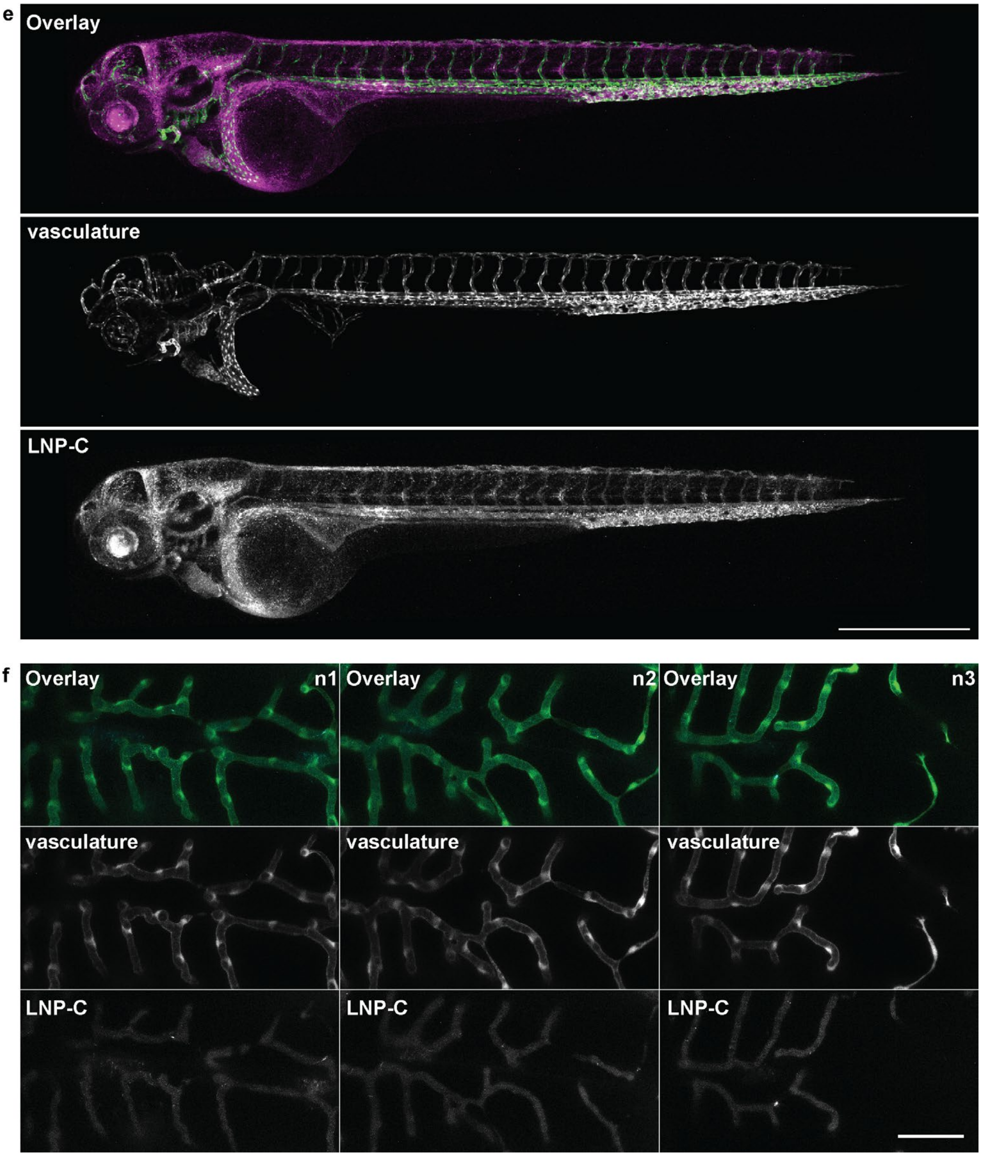
e
Overlay
vasculature
LNP-C
f
Overlay
n1
Overlay
n2
Overlay
n3
vasculature
vasculature
vasculature
LNP-C
LNP-C
LNP-C

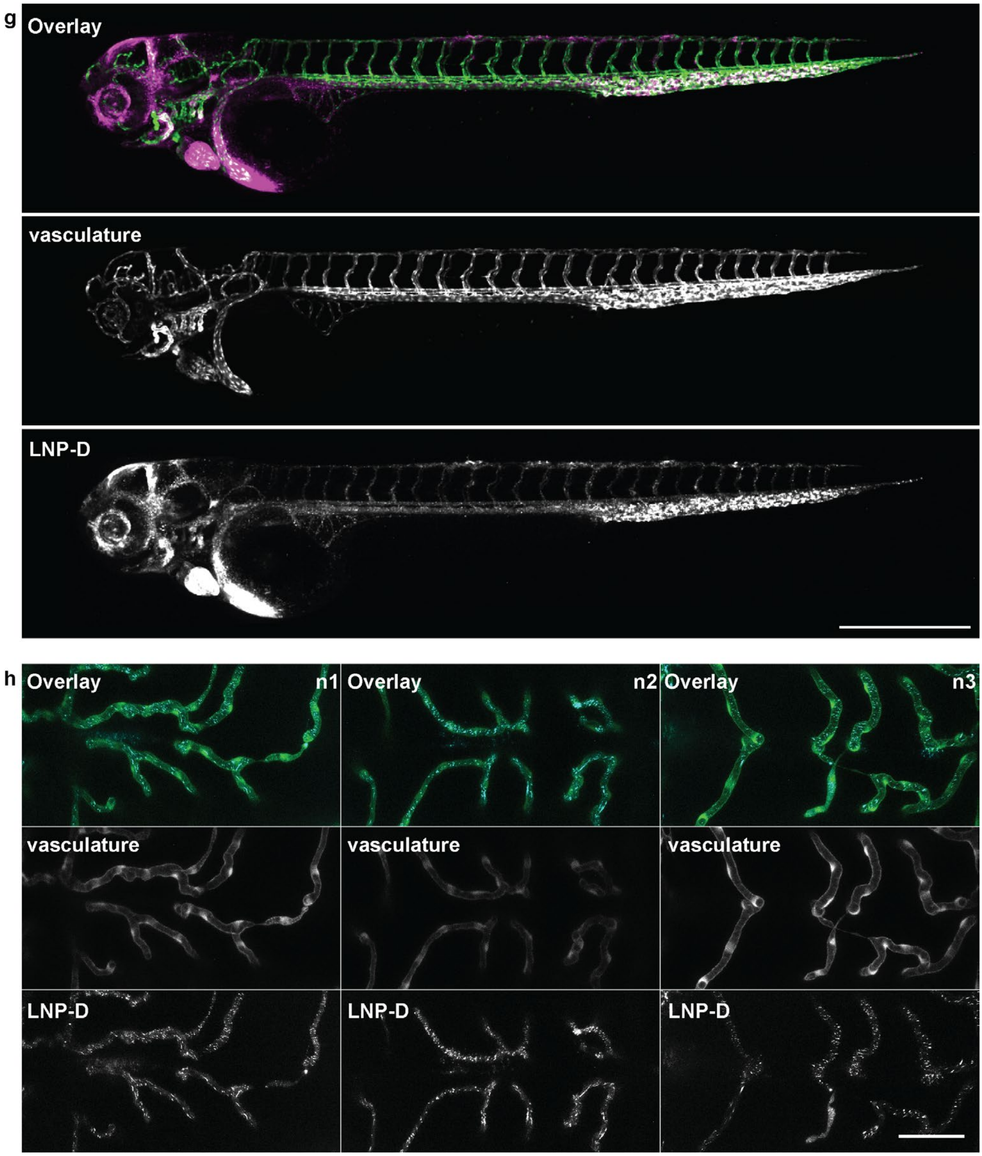

Figure S3. Biodistribution studies of LNP-A (**a, b**), -B (**c, d**), -C (**e, f**), and -D (**g, h**), in which (**a, c, e, g**) represent LNP biodistribution in lateral view on whole embryo, whereas (**b, d, f, h**) represent dorsal view on brain vasculature and LNP localization. Scale bars: 500 µm (a, c, e, g) and 50 µm (b, d, f, h).

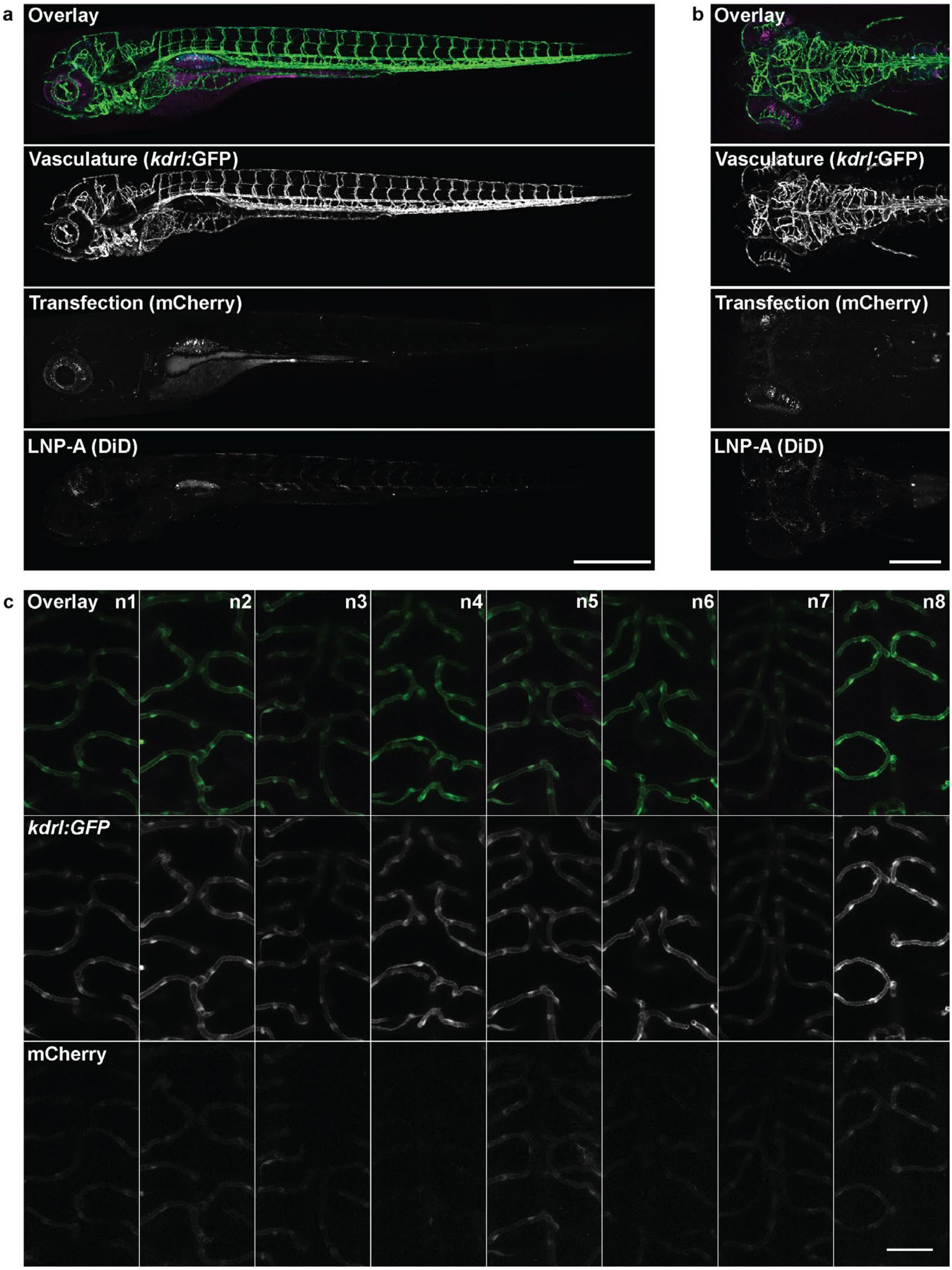
a
Overlay
Vasculature (*kdrl*:GFP)
Transfection (mCherry)
LNP-A (DiD)
b
Overlay
Vasculature (*kdrl*:GFP)
Transfection (mCherry)
LNP-A (DiD)
c
Overlay
n1
n2
n3
n4
n5
n6
n7
n8
kdrl:GFP
mCherry

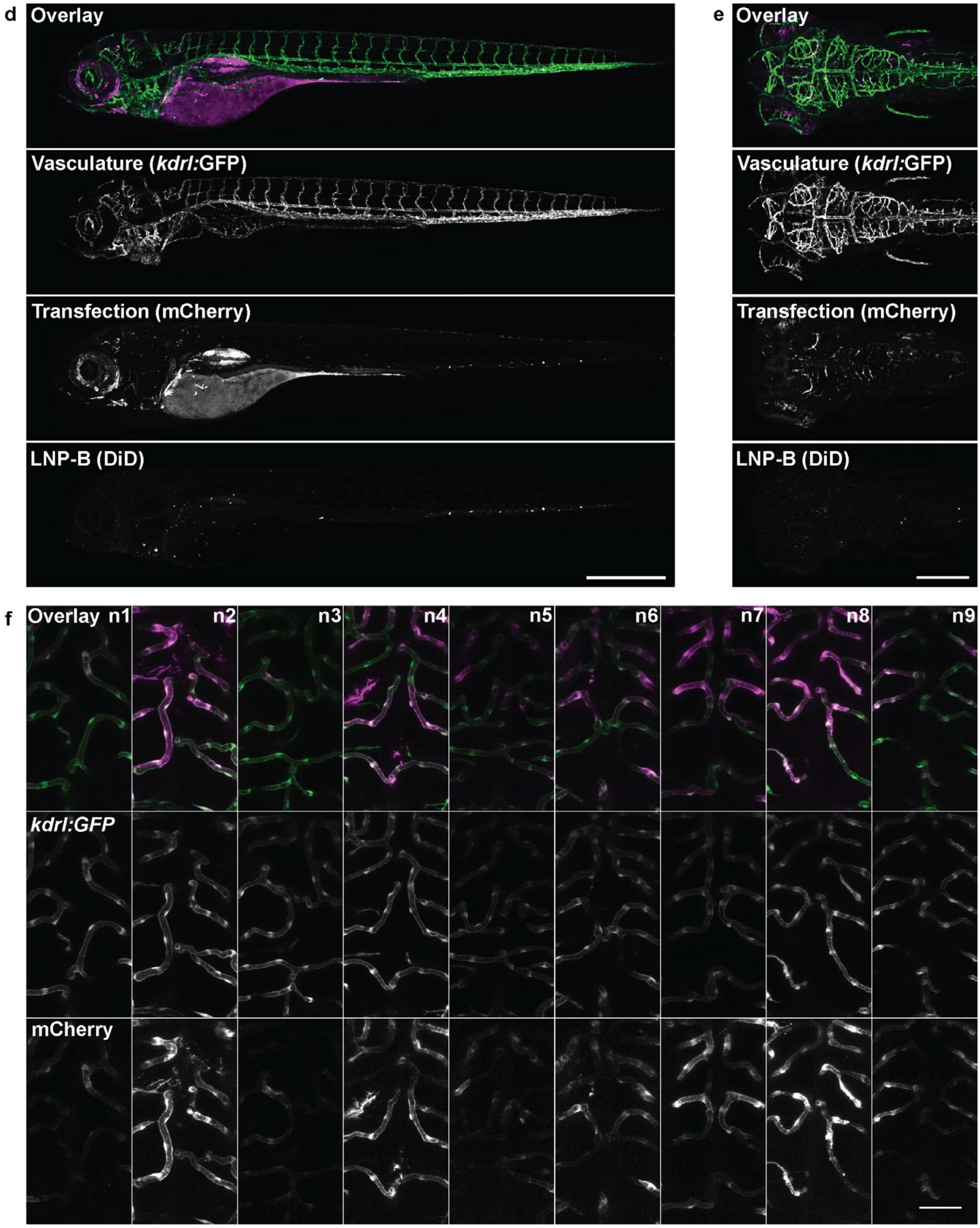
d
Overlay
Vasculature (*kdrl*:GFP)
Transfection (mCherry)
LNP-B (DiD)
e
Overlay
Vasculature (*kdrl*:GFP)
Transfection (mCherry)
LNP-B (DiD)
f
Overlay
n1
n2
n3
n4
n5
n6
n7
n8
n9
kdrl:GFP
mCherry

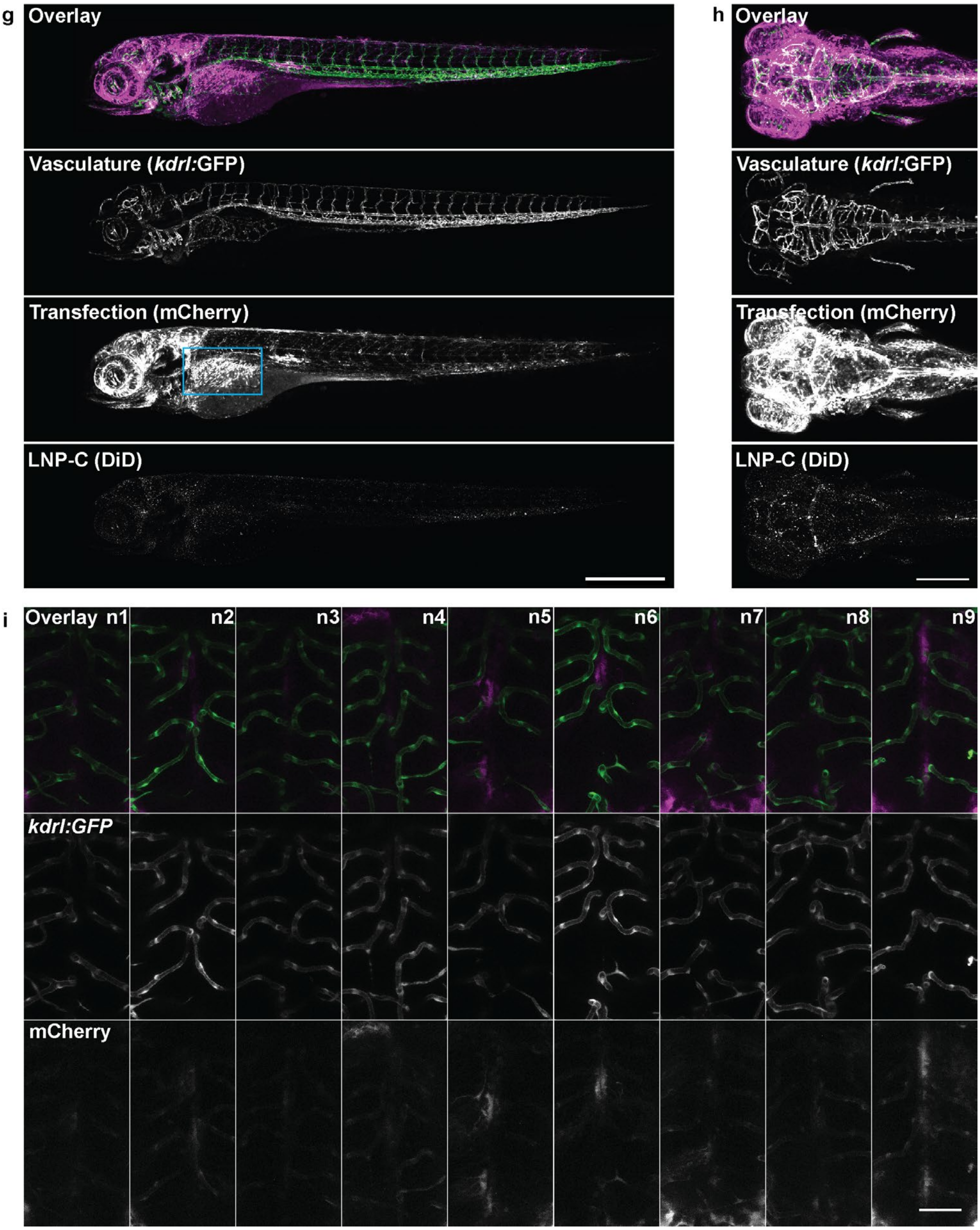
g
Overlay
Vasculature (*kdrl*:GFP)
Transfection (mCherry)
LNP-C (DiD)
h
Overlay
Vasculature (*kdrl*:GFP)
Transfection (mCherry)
LNP-C (DiD)
i
Overlay
n1
n2
n3
n4
n5
n6
n7
n8
n9
kdrl:GFP
mCherry

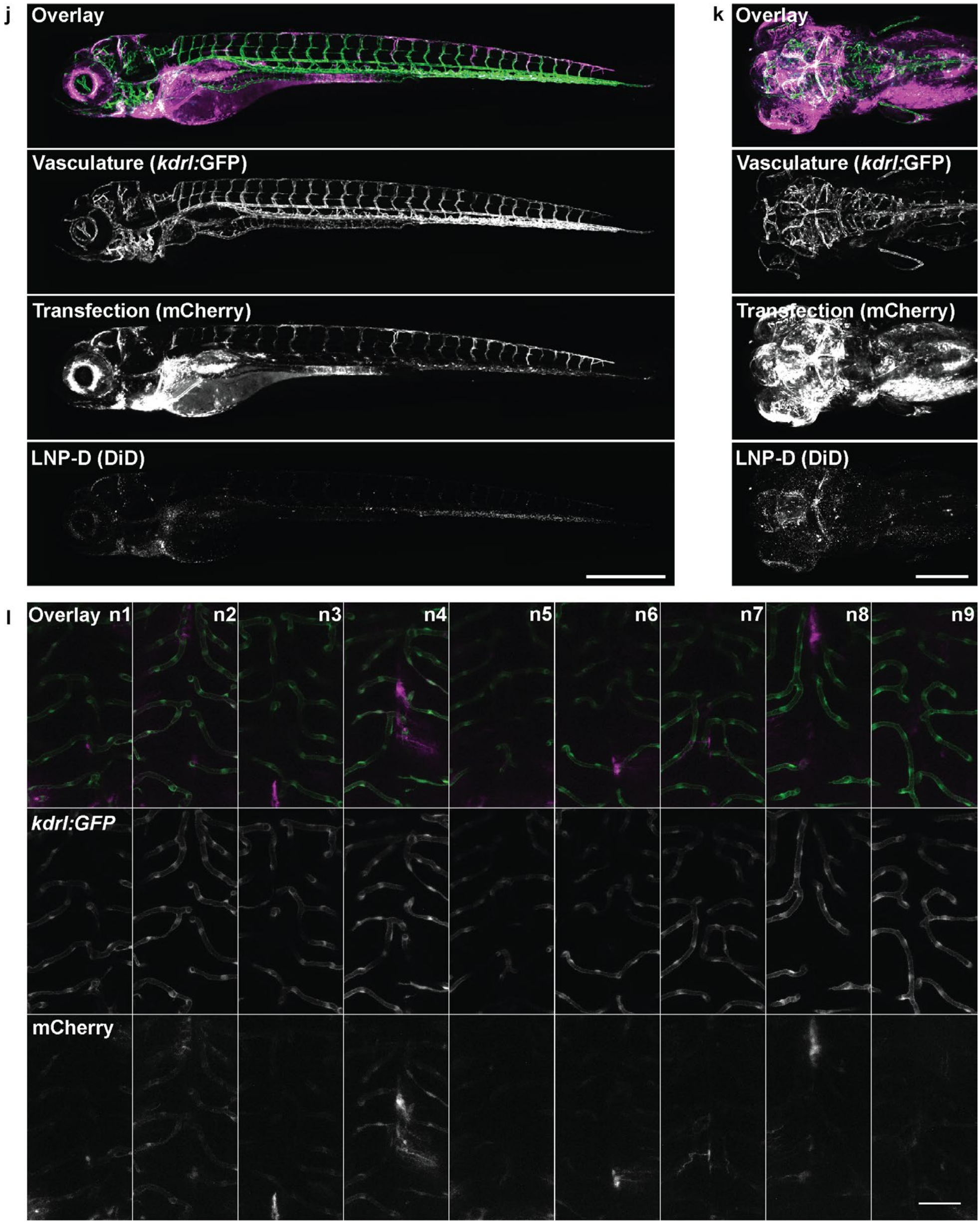

Figure S4. Transfection studies in zebrafish embryos as resulted from 36-38 hpi injected LNP-A (**a**-**c**), B (**d**-**f**), C (**g**-**i**), and D (**j**-**l**) in which (**a, d, g, j**) represent lateral whole embryo biodistribution and transfection, (**b, e, h, k**) represent dorsal biodistribution and transfection in zebrafish head region, and (**c, f, i, l**) display dorsal view on brain vasculature and transfection levels. Blue box in g indicates the liver/swim bladder. Scale bars: 500 µm (a, d, g, j), 250 µm (b, e, h, k), and 50 µm (c, f, i, l).

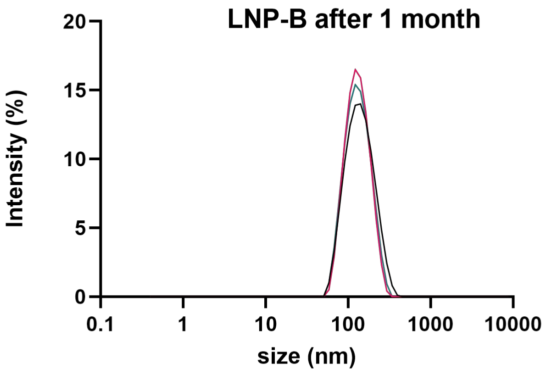

Figure S5. Stability of LNP-B. LNP-B as measured by DLS 1 month after formulation. Average diameter: 124.4 nm, PDI: 0.103.

Image acquisition and settings

Lateral: Leica SP8, 10X 0.4NA magnification, HyD detector

Dorsal: Leica SP8, 10X 0.4NA or 40X 0.8NA magnification, HyD detector

GFP detection: 488 nm laser excitation in 506-526 nm emission window

mCherry detection: 552 nm laser excitation in 600-620 nm emission window

DiD detection: 638 nm laser excitation in 650-670 nm emission window

Lateral: 1024x800 pixels, zoom 1.0, image speed 400, z-step 3.6 um, pinhole 1.0

Dorsal: 1024x500 pixels, zoom 1.28, image speed 700, z-step 3.6 um, pinhole 1.0

Stored as: ‘20210428 kdrlGFP 3.5dpf formulations bbbtargeting 18mM 4hpi DiD (2)’

Fiji Image reconstruction

For 4 hpi, DiD vs GFP colocalization

```
rename("stack1");
run("Make Substack...", "channels=1,3 slices=1-45");
run("Split Channels");
close("stack1");
run("JACoP ");
selectWindow("C2-stack1-1");
```

```
selectWindow("C1-stack1-1");
selectWindow("C2-stack1-1");
selectWindow("C1-stack1-1");
run("JACoP ", "imga=C1-stack1-1 imgb=C2-stack1-1 thra=50 thrb=130 pearson mm");
```

For 38 hpi, mCherry vs GFP colocalization

```
run("Make Substack...", "channels=1,3 slices=1-43");
run("Z Project...", "projection=[Max Intensity]");
Stack.setDisplayMode("grayscale");
run("Split Channels");
//for quantification mCherry, use 'Sum slices' instead of 'Max Intensity', and only make substack of mCherry (e.g., channel 3)
run("Make Substack...", "channels=3 slices=1-43");
run("Z Project...", "projection=[Sum Slices]");
//save images, make merges and montages for supplementary information, close images
//Open GFP positive image to create mask for specific endothelial cell colocalization
setOption("BlackBackground", false);
run("Convert to Mask");
run("Dilate");
run("Despeckle");
run("Divide...", "value=255");
//Open mCherry positive image
run("Image Calculator...");
//Multiply GFP mask from mCherry positive image
```

5.6 References

1. Kulkarni, J. A.; Witzigmann, D.; Thomson, S. B.; Chen, S.; Leavitt, B. R.; Cullis, P. R.; van der Meel, R. The Current Landscape of Nucleic Acid Therapeutics. *Nat Nanotechnol* **2021**, *16* (6), 630–643.
2. Springer, A. D.; Dowdy, S. F. GalNAc-siRNA Conjugates: Leading the Way for Delivery of RNAi Therapeutics. *Nucleic Acid Ther* **2018**, *28* (3), 109–118.
3. Nair, J. K.; Willoughby, J. L. S.; Chan, A.; Charisse, K.; Alam, M. R.; Wang, Q.; Hoekstra, M.; Kandasamy, P.; Kelin, A. V.; Milstein, S.; Taneja, N.; Oshea, J.; Shaikh, S.; Zhang, L.; Van Der Sluis, R. J.; Jung, M. E.; Akinc, A.; Hutabarat, R.; Kuchimanchi, S.; Fitzgerald, K.; Zimmermann, T.; Van Berkel, T. J. C.; Maier, M. A.; Rajeev, K. G.; Manoharan, M. Multivalent N -Acetylgalactosamine-Conjugated siRNA Localizes in Hepatocytes and Elicits Robust RNAi-Mediated Gene Silencing. *J Am Chem Soc* **2014**, *136* (49), 16958–16961.
4. Tsui, N. B. Y.; Ng, E. K. O.; Dennis Lo, Y. M. Stability of Endogenous and Added RNA in Blood Specimens, Serum, and Plasma. *Clin Chem* **2002**, *48* (10), 1647–1653.
5. Probst, J.; Brechtel, S.; Scheel, B.; Herr, I.; Jung, G.; Rammensee, H. G.; Pascolo, S. Characterization of the Ribonuclease Activity on the Skin Surface. *Genet Vaccines Ther* **2006**, *4* (1), 1–9.
6. Qin, S.; Tang, X.; Chen, Y.; Chen, K.; Fan, N.; Xiao, W.; Zheng, Q.; Li, G.; Teng, Y.; Wu, M.; Song, X. mRNA-Based Therapeutics: Powerful and Versatile Tools to Combat Diseases. *Signal Transduct Target Ther* **2022**, *7* (1), 166.
7. Khurana, A.; Allawadhi, P.; Khurana, I.; Allwadhi, S.; Weiskirchen, R.; Banothu, A. K.; Chhabra, D.; Joshi, K.; Bharani, K. K. Role of Nanotechnology behind the Success of mRNA Vaccines for COVID-19. *Nano Today* **2021**, *38*, 101142.
8. Pardi, N.; Tuyishime, S.; Muramatsu, H.; Kariko, K.; Mui, B. L.; Tam, Y. K.; Madden, T. D.; Hope, M. J.; Weissman, D. Expression Kinetics of Nucleoside-Modified mRNA Delivered in Lipid Nanoparticles to Mice by Various Routes. *J Control Release* **2015**, *217*, 345-351.
9. Szabó, G. T.; Mahiny, A. J.; Vlatkovic, I. COVID-19 mRNA Vaccines: Platforms and Current Developments. *Mol Ther* **2022**, *30* (5), 1850–1868.
10. Schoenmaker, L.; Witzigmann, D.; Kulkarni, J. A.; Verbeke, R.; Kersten, G.; Jiskoot, W.; Crommelin, D. J. A. mRNA-Lipid Nanoparticle COVID-19 Vaccines: Structure and Stability. *Int J Pharm* **2021**, *601*, 120586.

11. Tenchov, R.; Bird, R.; Curtze, A. E.; Zhou, Q. Lipid Nanoparticles from Liposomes to mRNA Vaccine Delivery, a Landscape of Research Diversity and Advancement. *ACS Nano* **2021**, *15* (11), 16982–17015.
12. Li, S.; Hu, Y.; Li, A.; Lin, J.; Hsieh, K.; Schneiderman, Z.; Zhang, P.; Zhu, Y.; Qiu, C.; Kokkoli, E.; Wang, T. H.; Mao, H. Q. Payload Distribution and Capacity of mRNA Lipid Nanoparticles. *Nat Commun* **2022**, *13* (1), 1–13.
13. Brader, M. L.; Williams, S. J.; Banks, J. M.; Hui, W. H.; Hong Zhou, Z.; Jin, L. Encapsulation State of Messenger RNA inside Lipid Nanoparticles. *Biophysj* **2021**, *120*, 2766–2770.
14. Patel, S.; Ashwanikumar, N.; Robinson, E.; Xia, Y.; Mihai, C.; Griffith, J. P.; Hou, S.; Esposito, A. A.; Ketova, T.; Welsher, K.; Joyal, J. L.; Almarsson, Ö.; Sahay, G. Naturally-Occurring Cholesterol Analogues in Lipid Nanoparticles Induce Polymorphic Shape and Enhance Intracellular Delivery of mRNA. *Nat Commun* **2020**, *11* (1), 1–13.
15. Eygeris, Y.; Patel, S.; Jozic, A.; Sahay, G.; Sahay, G. Deconvoluting Lipid Nanoparticle Structure for Messenger RNA Delivery. *Nano Lett* **2020**, *20* (6), 4543–4549.
16. Hald Albertsen, C.; Kulkarni, J. A.; Witzigmann, D.; Lind, M.; Petersson, K.; Simonsen, J. B. The Role of Lipid Components in Lipid Nanoparticles for Vaccines and Gene Therapy. *Adv Drug Deliv Rev* **2022**, *188*, 114416.
17. Da Silva Sanchez, A. J.; Zhao, K.; Huayamares, S. G.; Hatit, M. Z. C.; Lokugamage, M. P.; Loughrey, D.; Dobrowolski, C.; Wang, S.; Kim, H.; Paunovska, K.; Kuzminich, Y.; Dahlman, J. E. Substituting Racemic Ionizable Lipids with Stereopure Ionizable Lipids Can Increase mRNA Delivery. *J Control Release* **2023**, *353*, 270–277.
18. Hatit, M. Z. C.; Dobrowolski, C. N.; Lokugamage, M. P.; Loughrey, D.; Ni, H.; Zurla, C.; Da Silva Sanchez, A. J.; Radmand, A.; Huayamares, S. G.; Zenhausern, R.; Paunovska, K.; Peck, H. E.; Kim, J.; Sato, M.; Feldman, J. I.; Rivera, M. A.; Cristian, A.; Kim, Y. T.; Santangelo, P. J.; Dahlman, J. E. Nanoparticle Stereochemistry-Dependent Endocytic Processing Improves in Vivo mRNA Delivery. *Nat Chem 2023* **2023**, 1–8.
19. Stirland, D. L.; Nichols, J. W.; Miura, S.; Bae, Y. H. Mind the Gap: A Survey of How Cancer Drug Carriers Are Susceptible to the Gap between Research and Practice. *J Control Release* **2013**, *172* (3), 1045–1064.
20. Guidolin, K.; Zheng, G. Nanomedicines Lost in Translation. *ACS Nano* **2019**, *13* (12), 13620–13626.

21. Blanco, E.; Shen, H.; Ferrari, M. Principles of Nanoparticle Design for Overcoming Biological Barriers to Drug Delivery. *Nature Biotechnol* **2015**, *33* (9), 941-951.
22. Horejs, C. From Lipids to Lipid Nanoparticles to mRNA Vaccines. *Nat Rev Mater* **2021**, *6* (12), 1075-1076.
23. Allison, S. J.; Milner, J. Influence of Polyethylene Glycol Lipid Desorption Rates on Pharmacokinetics and Pharmacodynamics of siRNA Lipid Nanoparticles. *Mol Ther Nucleic Acids* **2013**, *2* (12), e139.
24. Pattipeiluhu, R.; Arias-Alpizar, G.; Basha, G.; Chan, K. Y. T.; Bussmann, J.; Sharp, T. H.; Moradi, M.-A.; Sommerdijk, N.; Harris, E. N.; Cullis, P. R.; Kros, A.; Witzigmann, D.; Campbell, F. Anionic Lipid Nanoparticles Preferentially Deliver mRNA to the Hepatic Reticuloendothelial System. *Adv Mater* **2022**, *34* (16), 2201095.
25. Patel, P.; Ibrahim, N. M.; Cheng, K. The Importance of Apparent pKa in the Development of Nanoparticles Encapsulating siRNA and mRNA. *Trends Pharmacol Sci* **2021**, *42* (6), 448–460.
26. Cullis, P. R.; Hope, M. J. Lipid Nanoparticle Systems for Enabling Gene Therapies. *Mol Ther* **2017**, *25* (7), 1467–1475.
27. Zheng, L.; Bandara, S. R.; Leal, C. Lipid Nanoparticle Topology Regulates Endosomal Escape and Delivery of RNA to the Cytoplasm. *PNAS* **2023**, *120* (27), e2301067120.
28. Liu, S.; Cheng, Q.; Wei, T.; Yu, X.; Johnson, L. T.; Farbiak, L.; Siegwart, D. J. Membrane-Destabilizing Ionizable Phospholipids for Organ-Selective mRNA Delivery and CRISPR–Cas Gene Editing. *Nat Mater* **2021**, *20* (5), 701–710.
29. Meng, N.; Grimm, D. Membrane-Destabilizing Ionizable Phospholipids: Novel Components for Organ-Selective mRNA Delivery and CRISPR–Cas Gene Editing. *Signal Transduct Target Ther* **2021**, *6* (1), 1–3.
30. Hafez, I. M.; Maurer, N.; Cullis, P. R. On the Mechanism Whereby Cationic Lipids Promote Intracellular Delivery of Polynucleic Acids. *Gene Ther* **2001**, *8* (15), 1188–1196.
31. Dowdy, S. F.; Setten, R. L.; Cui, X. S.; Jadhav, S. G. Delivery of RNA Therapeutics: The Great Endosomal Escape! *Nucleic Acid Ther* **2022**, *32* (5), 361–368.
32. Semple, S. C.; Klimuk, S. K.; Harasym, T. O.; Dos Santos, N.; Ansell, S. M.; Wong, K. F.; Maurer, N.; Stark, H.; Cullis, P. R.; Hope, M. J.; Scherrer, P. Efficient Encapsulation of Antisense Oligonucleotides in Lipid Vesicles Using Ionizable Aminolipids: Formation of Novel Small Multilamellar Vesicle Structures. *Biochim Biophys Acta - Biomembr* **2001**, *1510* (1–2), 152–166.

33. Jayaraman, M.; Ansell, S. M.; Mui, B. L.; Tam, Y. K.; Chen, J.; Du, X.; Butler, D.; Eltepu, L.; Matsuda, S.; Narayanannair, J. K.; Rajeev, K. G.; Hafez, I. M.; Akinc, A.; Maier, M. A.; Tracy, M. A.; Cullis, P. R.; Madden, T. D.; Manoharan, M.; Hope, M. J. Maximizing the Potency of siRNA Lipid Nanoparticles for Hepatic Gene Silencing In Vivo. *Angew Chem Int Ed Engl* **2012**, *51* (34), 8529-8533.
34. Semple, S. C.; Akinc, A.; Chen, J.; Sandhu, A. P.; Mui, B. L.; Cho, C. K.; Sah, D. W. Y.; Stebbing, D.; Crosley, E. J.; Yaworski, E.; Hafez, I. M.; Dorkin, J. R.; Qin, J.; Lam, K.; Rajeev, K. G.; Wong, K. F.; Jeffs, L. B.; Nechev, L.; Eisenhardt, M. L.; Jayaraman, M.; Kazem, M.; Maier, M. A.; Srinivasulu, M.; Weinstein, M. J.; Chen, Q.; Alvarez, R.; Barros, S. A.; De, S.; Klimuk, S. K.; Borland, T.; Kosovrasti, V.; Cantley, W. L.; Tam, Y. K.; Manoharan, M.; Ciufolini, M. A.; Tracy, M. A.; De Fougerolles, A.; MacLachlan, I.; Cullis, P. R.; Madden, T. D.; Hope, M. J. Rational Design of Cationic Lipids for siRNA Delivery. *Nat Biotechnol* **2010**, *28* (2), 172–176.
35. Ansell, S. M. Lipids and Lipid Nanoparticle Formulations for Delivery of Nucleic Acids. **2016**.
36. Hou, X.; Zaks, T.; Langer, R.; Dong, Y. Lipid Nanoparticles for mRNA Delivery. *Nat Rev Mater* **2021**, *6* (12), 1078–1094.
37. Kulkarni, J. A.; Witzigmann, D.; Leung, J.; Tam, Y. Y. C.; Cullis, P. R. On the Role of Helper Lipids in Lipid Nanoparticle Formulations of siRNA. *Nanoscale* **2019**, *11* (45), 21733–21739.
38. Veatch, S. L.; Keller, S. L. Separation of Liquid Phases in Giant Vesicles of Ternary Mixtures of Phospholipids and Cholesterol. *Biophys J* **2003**, *85* (5), 3074–3083.
39. Tenchov, B. G.; MacDonald, R. C.; Siegel, D. P. Cubic Phases in Phosphatidylcholine-Cholesterol Mixtures: Cholesterol as Membrane "Fusogen." *Biophys J* **2006**, *91* (7), 2508–2516.
40. Alwarawrah, M.; Dai, J.; Huang, J. Modification of Lipid Bilayer Structure by Diacylglycerol: A Comparative Study of Diacylglycerol and Cholesterol. *J Chem Theory Comput* **2012**, *8* (2), 749–758.
41. Vieu, C.; Jaspard, B.; Barbaras, R.; Manent, J.; Chap, H.; Perret, B.; Collet, X. Identification and Quantification of Diacylglycerols in HDL and Accessibility to Lipase. *J Lipid Res* **1996**, *37* (5), 1153–1161.
42. Coffill, C. R.; Ramsamy, T. A.; Hutt, D. M.; Schultz, J. R.; Sparks, D. L. Diacylglycerol Is the Preferred Substrate in High Density Lipoproteins for Human Hepatic Lipase. *J Lipid Res* **1997**, *38* (11), 2224–2231.

43. Goñi, F. M.; Alonso, A. Structure and Functional Properties of Diacylglycerols in Membranes. *Prog Lipid Res* **1999**, *38* (1), 1–48.

44. Bilayers Edward Goldberg, P. M.; Lester, D. S.; Borchardt, D. B.; Zidovetzki, R. Effects of Diacylglycerols and Ca2+ on Structure of Phosphatidylcholine/Phosphatidylserine Bilayers. *Biophys J* **1994**, *66*, 382–393.

45. Dawson, R. M. C.; Hemington, N. L.; Irvine, R. F. Diacylglycerol Potentiates Phospholipase Attack upon Phospholipid Bilayers: Possible Connection with Cell Stimulation. *Biochem Biophys Res Commun* **1983**, *117* (1), 196–201.

46. Heinonen, S.; Lautala, S.; Koivuniemi, A.; Bunker, A. Insights into the Behavior of Unsaturated Diacylglycerols in Mixed Lipid Bilayers in Relation to Protein Kinase C Activation—A Molecular Dynamics Simulation Study. *Biochim Biophys Acta - Biomembr* **2022**, *1864* (9), 183961.

47. Alwarawrah, M.; Hussain, F.; Huang, J. Alteration of Lipid Membrane Structure and Dynamics by Diacylglycerols with Unsaturated Chains. *Biochim Biophys Acta - Biomembr* **2016**, *1858* (2), 253–263.

48. Campomanes, P.; Zoni, V.; Vanni, S. Local Accumulation of Diacylglycerol Alters Membrane Properties Nonlinearly Due to Its Transbilayer Activity. *Commun Chem* **2019**, *2* (1), 1–8.

49. Basáñez, G.; Nieva, J. L.; Rivas, E.; Alonso, A.; Goñi, F. M. Diacylglycerol and the Promotion of Lamellar-Hexagonal and Lamellar-Isotropic Phase Transitions in Lipids: Implications for Membrane Fusion. *Biophys J* **1996**, *70* (5), 2299–2306.

50. Arias-Alpizar, G.; Papadopoulou, P.; Rios, X.; Pulagam, K. R.; Moradi, M. A.; Pattipeiluhu, R.; Bussmann, J.; Sommerdijk, N.; Llop, J.; Kros, A.; Campbell, F. Phase-Separated Liposomes Hijack Endogenous Lipoprotein Transport and Metabolism Pathways to Target Subsets of Endothelial Cells In Vivo. *Adv Healthc Mater* **2023**, *12* (10), e2202709.

51. Papadopoulou, P.; Van Der Pol, R.; Van Hilten, N.; Moradi, M.-A.; Ferraz, M. J.; Aerts, J. M. F. G.; Sommerdijk, N.; Risselada, H. J.; Sevink, G. J. A.; Kros, A. Lipase-Mediated Selective Hydrolysis of Lipid Droplets in Phase Separated-Liposomes. *ChemRxiv* **2023**.

52. Leung, A. K. K.; Tam, Y. C.; Chen, S.; Hafez, I. M.; Cullis, P. R. Microfluidic Mixing: A General Method for Encapsulating Macromolecules in Lipid Nanoparticle Systems. *J. Phys. Chem. B* **2015**, *119* (28), 8698-8706.

53. Arteta, M. Y.; Kjellman, T.; Bartesaghi, S.; Wallin, S.; Wu, X.; Kvist, A. J.; Dabkowska, A.; Székely, N.; Radulescu, A.; Bergenholtz, J.; Lindfors, L. Successful

Reprogramming of Cellular Protein Production through mRNA Delivered by Functionalized Lipid Nanoparticles. *PNAS* **2018**, *115* (15), E3351–E3360.

54. Manders, E. M. M.; Verbeek, F. J.; Aten, J. A. Measurement of Co-Localization of Objects in Dual-Colour Confocal Images. *J Microsc* **1993**, *169* (3), 375–382.

55. Cheng, M. H. Y.; Leung, J.; Zhang, Y.; Strong, C.; Basha, G.; Momeni, A.; Chen, Y.; Jan, E.; Abdolahzadeh, A.; Wang, X.; Kulkarni, J. A.; Witzigmann, D.; Cullis, P. R. Induction of Bleb Structures in Lipid Nanoparticle Formulations of mRNA Leads to Improved Transfection Potency. *Adv Mater* **2023**, e2303370.

56. Arias-Alpizar, G.; Kong, L.; Vlieg, R. C.; Rabe, A.; Papadopoulou, P.; Meijer, M. S.; Bonnet, S.; Vogel, S.; van Noort, J.; Kros, A.; Campbell, F. Light-Triggered Switching of Liposome Surface Charge Directs Delivery of Membrane Impermeable Payloads in Vivo. *Nat Commun* **2020**, *11*, 3638.

57. Sieber, S.; Grossen, P.; Bussmann, J.; Campbell, F.; Kros, A.; Witzigmann, D.; Huwyler, J. Zebrafish as a Preclinical in Vivo Screening Model for Nanomedicines. *Adv Drug Deliv Rev* **2019**, *151–152*, 152–168.

58. Arias-Alpizar, G.; Bussmann, J.; Campbell, F. Zebrafish Embryos as a Predictive Animal Model to Study Nanoparticle Behavior in Vivo. *Bio Protoc* **2021**, *11* (19), e4173.

59. Hatit, M. Z. C.; Lokugamage, M. P.; Dobrowolski, C. N.; Paunovska, K.; Ni, H.; Zhao, K.; Vanover, D.; Beyersdorf, J.; Peck, H. E.; Loughrey, D.; Sato, M.; Cristian, A.; Santangelo, P. J.; Dahlman, J. E. Species-Dependent in vivo mRNA Delivery and Cellular Responses to Nanoparticles. *Nat Nanotechnol* **2022**, *17* (3), 310–318.

60. Sevigny, J.; Chiao, P.; Bussière, T.; Weinreb, P. H.; Williams, L.; Maier, M.; Dunstan, R.; Salloway, S.; Chen, T.; Ling, Y.; O'Gorman, J.; Qian, F.; Arastu, M.; Li, M.; Chollate, S.; Brennan, M. S.; Quintero-Monzon, O.; Scannevin, R. H.; Arnold, H. M.; Engber, T.; Rhodes, K.; Ferrero, J.; Hang, Y.; Mikulskis, A.; Grimm, J.; Hock, C.; Nitsch, R. M.; Sandrock, A. The Antibody Aducanumab Reduces Aβ Plaques in Alzheimer's Disease. *Nature* **2016**, *537* (7618), 50–56.

61. Mitra, S.; Behbahani, H.; Eriksdotter, M. Innovative Therapy for Alzheimer's Disease-with Focus on Biodelivery of NGF. *Front Neurosci* **2019**, *13*, 38.

62. Chen, X.; Wolfe, D. A.; Bindu, D. S.; Zhang, M.; Taskin, N.; Goertsen, D.; Shay, T. F.; Sullivan, E. E.; Huang, S. F.; Ravindra Kumar, S.; Arokiaraj, C. M.; Plattner, V. M.; Campos, L. J.; Mich, J. K.; Monet, D.; Ngo, V.; Ding, X.; Omstead, V.; Weed, N.; Bishaw, Y.; Gore, B. B.; Lein, E. S.; Akrami, A.; Miller, C.; Levi, B. P.; Keller, A.; Ting, J. T.; Fox, A. S.; Eroglu, C.; Gradinaru, V. Functional Gene Delivery to and

across Brain Vasculature of Systemic AAVs with Endothelial-Specific Tropism in Rodents and Broad Tropism in Primates. *Nat Commun* **2023**, *14* (1), 1–19.

63. Weiss, N.; Miller, F.; Cazaubon, S.; Couraud, P. O. The Blood-Brain Barrier in Brain Homeostasis and Neurological Diseases. *Biochim Biophys Acta - Biomembr* **2009**, *1788* (4), 842–857.
64. Mastronarde, D. N. Automated Electron Microscope Tomography Using Robust Prediction of Specimen Movements. *J Struct Biol* **2005**, *152* (1), 36–51.
65. Kremer, J. R.; Mastronarde, D. N.; McIntosh, J. R. Computer Visualization of Three-Dimensional Image Data Using IMOD. *J Struct Biol* **1996**, *116* (1), 71–76.
66. Jin, S. W.; Beis, D.; Mitchell, T.; Chen, J. N.; Stainier, D. Y. R. Cellular and Molecular Analyses of Vascular Tube and Lumen Formation in Zebrafish. *Development* **2005**, *132* (23), 5199–5209.
67. Campbell, F.; Bos, F. L.; Sieber, S.; Arias-Alpizar, G.; Koch, B. E.; Huwyler, J.; Kros, A.; Bussmann, J. Directing Nanoparticle Biodistribution through Evasion and Exploitation of Stab2-Dependent Nanoparticle Uptake. *ACS Nano* **2018**, *12* (3), 2138-2150.
68. Bolte, S.; Cordelières, F. P. A Guided Tour into Subcellular Colocalization Analysis in Light Microscopy. *J Microsc* **2006**, *224* (3), 213–232.